

# UC Berkeley

## UC Berkeley Previously Published Works

### Title

Surface slip during large Owens Valley earthquakes

### Permalink

<https://escholarship.org/uc/item/5hq131rg>

### Journal

Geochemistry Geophysics Geosystems, 17(6)

### ISSN

1525-2027

### Authors

Haddon, EK  
Amos, CB  
Zielke, O  
[et al.](#)

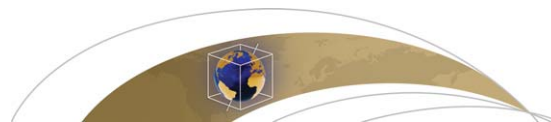
### Publication Date

2016-06-01

### DOI

10.1002/2015gc006033

Peer reviewed



## RESEARCH ARTICLE

## Surface slip during large Owens Valley earthquakes

10.1002/2015GC006033

E. K. Haddon<sup>1,2</sup>, C. B. Amos<sup>1</sup>, O. Zielke<sup>3</sup>, A. S. Jayko<sup>4</sup>, and R. Bürgmann<sup>5</sup>

### Key Points:

- Geomorphic characterization of offset landforms along the Owens Valley fault
- Quantifying lateral geomorphic offsets using cross-correlation and field data
- Characterization of three large earthquakes

### Supporting Information:

- Supporting Information S1
- Table S1
- Table S2
- Table S3
- Table S4
- Table S5
- Data Set S1
- Data Set S2
- Data Set S3
- Data Set S4
- Software S1

### Correspondence to:

E. K. Haddon,  
b.haddon@gmail.com

### Citation:

Haddon, E. K., C. B. Amos, O. Zielke, A. S. Jayko, and R. Bürgmann (2016), Surface slip during large Owens Valley earthquakes, *Geochem. Geophys. Geosyst.*, 17, doi:10.1002/2015GC006033.

Received 4 AUG 2015

Accepted 4 JAN 2016

Accepted article online 8 JAN 2016

<sup>1</sup>Geology Department, Western Washington University, Bellingham, Washington, USA, <sup>2</sup>Now at Department of Earth and Climate Science, San Francisco State University, San Francisco, CA, USA, <sup>3</sup>Department of Earth Science and Engineering, King Abdullah University of Science and Technology, Thuwal, Saudi Arabia, <sup>4</sup>U.S. Geological Survey, White Mountain Research Center, Bishop, California, USA, <sup>5</sup>Department of Earth and Planetary Science, Berkeley Seismological Laboratory, University of California, Berkeley, California, USA

**Abstract** The 1872 Owens Valley earthquake is the third largest known historical earthquake in California. Relatively sparse field data and a complex rupture trace, however, inhibited attempts to fully resolve the slip distribution and reconcile the total moment release. We present a new, comprehensive record of surface slip based on lidar and field investigation, documenting 162 new measurements of laterally and vertically displaced landforms for 1872 and prehistoric Owens Valley earthquakes. Our lidar analysis uses a newly developed analytical tool to measure fault slip based on cross-correlation of sublinear topographic features and to produce a uniquely shaped probability density function (PDF) for each measurement. Stacking PDFs along strike to form cumulative offset probability distribution plots (COPDs) highlights common values corresponding to single and multiple-event displacements. Lateral offsets for 1872 vary systematically from  $\sim 1.0$  to  $6.0$  m and average  $3.3 \pm 1.1$  m ( $2\sigma$ ). Vertical offsets are predominantly east-down between  $\sim 0.1$  and  $2.4$  m, with a mean of  $0.8 \pm 0.5$  m. The average lateral-to-vertical ratio compiled at specific sites is  $\sim 6:1$ . Summing displacements across subparallel, overlapping rupture traces implies a maximum of  $7\text{--}11$  m and net average of  $4.4 \pm 1.5$  m, corresponding to a geologic  $M_w \sim 7.5$  for the 1872 event. We attribute progressively higher-offset lateral COPD peaks at  $7.1 \pm 2.0$  m,  $12.8 \pm 1.5$  m, and  $16.6 \pm 1.4$  m to three earlier large surface ruptures. Evaluating cumulative displacements in context with previously dated landforms in Owens Valley suggests relatively modest rates of fault slip, averaging between  $\sim 0.6$  and  $1.6$  mm/yr ( $1\sigma$ ) over the late Quaternary.

## 1. Introduction

Characterizing the distribution of surface slip during large earthquakes provides important insights into crustal dynamics, controls on rupture propagation, and earthquake recurrence [e.g., Wells and Coppersmith, 1994]. An increasing inventory of well-described historical ruptures constrains physical parameters such as the slip-to-rupture-length ratio for historical earthquakes in a variety of plate tectonic settings [e.g., Wesnousky, 2008; Stirling et al., 2013]. Improved slip-length scaling relations provide a framework for evaluating measurement biases and uncertainties for pre-instrumental data sets (pre-1900s) [e.g., Stirling et al., 2002] and the potential influence of structural maturity on static stress changes [e.g., Hecker et al., 2010]. Recent studies demonstrate patterns of surface slip during large earthquake ruptures that may depend on fault strength [e.g., Griffith et al., 2009; Candela et al., 2011], fault geometry [e.g., Wesnousky, 1988; Klinger et al., 2006; Manighetti et al., 2005; Klinger, 2010], and stress interactions [e.g., Gupta and Scholz, 2000; Scholz and Lawler, 2004; Rockwell and Klinger, 2013]. These studies suggest physical bases for spatial and temporal patterns of geologic deformation accrued over multiple earthquake cycles, aiding distinction among predictive models for strain release and earthquake recurrence (e.g., the variable slip, uniform slip, and characteristic earthquake models) [Sieh and Jahns, 1984; Schwartz and Coppersmith, 1984].

Advances in the ability to image and analyze active faults using high-resolution lidar topography and imagery provide an opportunity to map earthquake surface ruptures with unprecedented detail [e.g., Oskin et al., 2012; Duffy et al., 2013] and improve upon existing field catalogs of geomorphic offset [e.g., Zielke et al., 2015]. In some cases, reinterpreted surface slip distributions offer new perspectives on patterns of earthquake slip and recurrence [e.g., Zielke et al., 2012; Madden et al., 2013]. Much of this recent work focuses on plate boundary faults, however, that exhibit relatively high slip rates and comparatively short

earthquake recurrence intervals, such as the San Andreas and Imperial fault systems in southern California [e.g., Zielke *et al.*, 2010; Madden *et al.*, 2013; Rockwell and Klinger, 2013]. Given the relative frequency of large earthquakes ( $\sim 10^{-2}$  year) in comparison with the pace of landform development in such locations, tectonic-geomorphic investigations face the challenge of a potentially incomplete geomorphic record of past surface ruptures [e.g., Sieh, 1978; Sieh and Jahns, 1984; Zielke *et al.*, 2010; Ludwig *et al.*, 2010; Akçiz *et al.*, 2010; Zielke *et al.*, 2015].

The Owens Valley fault (OVF) (Figure 1) represents an intracontinental structure located within a distributed zone of Pacific–North American plate boundary deformation. The OVF experiences large but relatively infrequent earthquakes ( $\sim 10^{-3}$  to  $10^{-4}$  year) involving predominantly right-lateral slip [e.g., Beanland and Clark, 1994; Lee *et al.*, 2001a; Bacon and Pezzopane, 2007]. Although geologic slip estimates range upward of  $\sim 3$ – $5$  mm/yr [Kirby *et al.*, 2008], previous studies mainly suggest Quaternary-to-recent slip rates  $\leq \sim 2$  mm/yr [e.g., Dixon *et al.*, 2003]. The March 26, 1872 Owens Valley earthquake ruptured multiple geometric fault segments, generating a complex surface rupture trace similar to the 1992  $M_w$  7.3 Landers and 1999  $M_w$  7.1 Hector Mine earthquakes (Figure 1) [Sieh *et al.*, 1993; Treiman *et al.*, 2002]. Early investigation of the 1872 earthquake surface slip distribution noted high average and maximum lateral surface displacements ( $\sim 4$ – $6$  and  $7$ – $11$  m, respectively) [Lubetkin and Clark, 1988; Vittori *et al.*, 1993; Beanland and Clark, 1994; McCalpin and Slemmons, 1998] with respect to the  $\sim 113$ – $120$  km rupture trace [Slemmons *et al.*, 2008; Amos *et al.*, 2013a], suggesting the 1872 Owens Valley earthquake was a high stress drop event [e.g., Hanks and Bakun, 2002]. Apparent discrepancies between estimates of 1872 magnitude from geologic observations ( $M_w$  7.5–7.7) [e.g., Beanland and Clark, 1994; Stein and Hanks, 1998] and interpretations of macroseismic accounts by Bakun [2006] ( $M_w$  7.4–7.5) and Hough and Hutton [2008] ( $M_w$  7.8–7.9) emphasize the importance of resolving fundamental rupture parameters, such as rupture length and average slip during OVF earthquakes. In addition, the relatively arid climate and well-preserved Owens Valley landscape combined with the comparatively long, millennial interseismic period ( $\sim 3$ – $10$  ka) [Lubetkin and Clark, 1988; Beanland and Clark, 1994; Bierman *et al.*, 1995; Lee *et al.*, 2001a; Bacon and Pezzopane, 2007] suggests the potential for a nearly continuous geomorphic archive of recent moderate to large earthquake surface ruptures, despite complexities in the surface rupture trace.

Here, we delineate spatial and temporal patterns of coseismic slip along the OVF and explore controls on rupture and moment release relevant during 1872 and earlier earthquakes. We revisit the surface rupture using high spatial resolution (25-cm) lidar topography and complementary field study. Our mapping and field investigations highlight previously unrecognized faulted landforms useful for reconstructions of surface slip along strike. We adopt a newly developed analysis tool based on cross-correlation to measure discrete lateral and vertical offset of sublinear geomorphic features. Our new and comprehensive database of 238 surface slip measurements includes 162 new measurements, 21 remeasured landforms, and 55 previously published field measurements that together: (1) expand the current number of field-verified geomorphic offset observations, largely documented pre-lidar; (2) constrain the amount and extent of surface slip during the most recent event (MRE) in 1872, as well as during the penultimate event (PE) and earlier earthquakes; (3) bracket the rate of fault slip averaged over various late Quaternary time intervals; (4) update geological estimates of moment release and magnitude during the 1872 Owens Valley earthquake; and (5) shed light on critical questions related to source parameters bearing on seismic hazards for similar faults in slowly deforming continental interiors.

## 2. Background

### 2.1. Geologic Setting

The OVF (Figure 1) represents one structure in a network of distributed strike-slip and normal faults forming the eastern boundary of the Sierra Nevada–Great Valley microplate [Unruh *et al.*, 2003] collectively termed the eastern California shear zone (ECSZ) or Walker Lane (WL) [e.g., Stewart, 1988; Wesnousky, 2005]. Geodetic measurements spanning this region indicate present-day dextral shear at  $10.6 \pm 0.5$  mm/yr [Lifton *et al.*, 2013], upward of 20% of the relative Pacific–North American plate motion [e.g., Dokka and Travis, 1990]. Contemporary background seismicity demonstrates that northwestward translation of the Sierra Nevada–Great Valley microplate drives deformation across this region [Unruh *et al.*, 2003]. Both discontinuous normal and strike-slip faults with potentially significant vertical axis rotations accommodate dextral

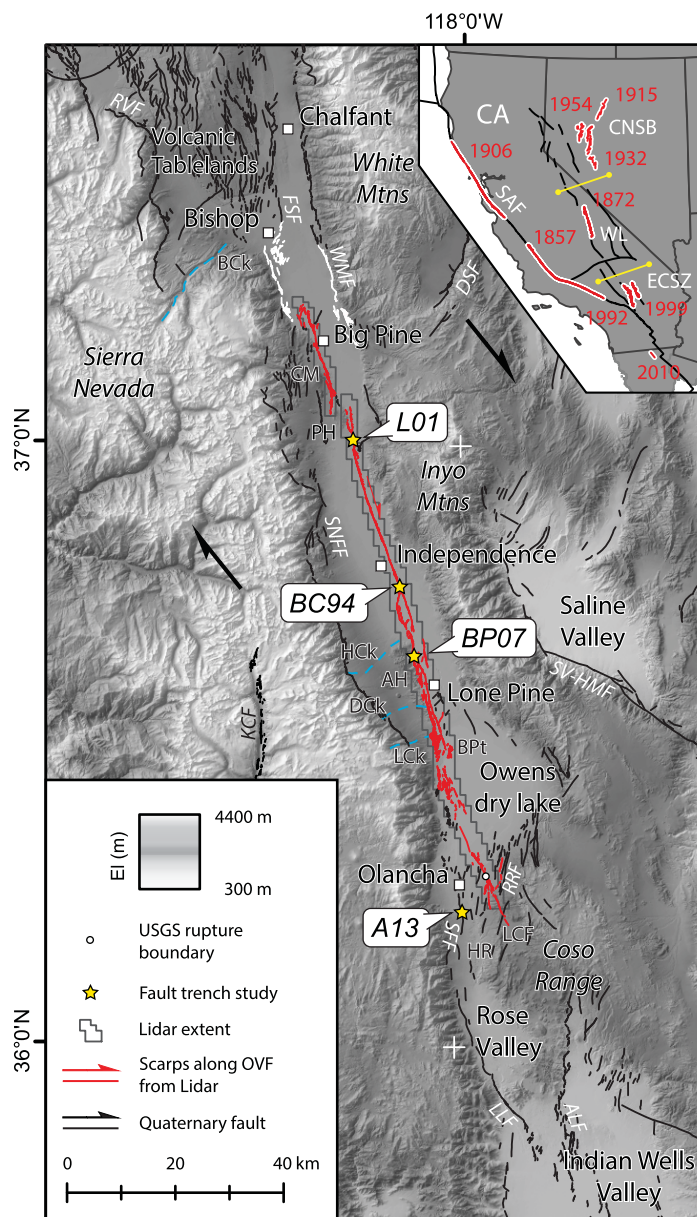


**Figure 1.** Regional overview of the Owens Valley fault including scarps mapped from EarthScope lidar. The mapped extent of the Keough section of the Sierra Nevada frontal fault (SNFF) and the most recent surface rupture of the White Mountain fault (WMF) [dePolo, 1989] appear white. Faults shown in black are from the U.S. Geological Survey Quaternary fault and fold database, with the exception of the Kern Canyon fault (KCF) from Brossy *et al.* [2012]. Surface slip measurements are at sites located with respect to the rupture boundary (white point), as specified in the U.S. Geological Survey database. Yellow stars indicate the location of paleoseismic trenches from previous studies. Black arrows indicate the azimuth of local plate boundary motion (N37°W) [Lifton *et al.*, 2013]. The inset provides regional context for the 1872 rupture in the Walker Lane (WL) or eastern California shear zone (ECSZ) with respect to several historical ruptures in California (e.g., the 1857 and 1906 San Andreas, 1992 Landers, and 1999 Hector Mine earthquakes), the Central Nevada Seismic Belt (CNSB) (e.g., 1915 Pleasant Valley, 1932 Cedar Mountain, 1954 Fairview Peak–Dixie Valley, and 1954 Rainbow Mountain–Stillwater), and Baja (2010 El Mayor Cucupah earthquake). Yellow transects indicate integrated slip from GPS across the WL and ECSZ at  $10.6 \pm 0.5$  mm/yr [Lifton *et al.*, 2013] and  $\sim 10$ – $12$  mm/yr, respectively [Dixon *et al.*, 1995; Sauber *et al.*, 1994]. Fault trench studies: A13, Amos *et al.* [2013a]; BP07, Bacon and Pezzopane [2007]; BC94, Beanland and Clark [1994]; and L01, Lee *et al.* [2001a]. Geographic locations: AH, Alabama Hills; ALF, Airport Lake fault; BCK, Bishop Creek; BPT, Bartlett Point; CA, California; CM, Crater Mountain; DSF, Deep Springs fault; DCK, Diaz Creek; ECSZ, eastern California shear zone; FSF, Fish Slough fault; HCK, Hogback Creek fan; HR, Haiwee reservoir; KCF, Kern Canyon fault; LCF, Lower Cactus flat; LCK, Lubken Creek; LLF, Little Lake fault; PH, Poverty Hills; RRF, Red Ridge fault; RVF, Round Valley fault; SAF, San Andreas fault; SFF, Sage Flat fault; SV–HMF, Saline Valley–Hunter Mountain fault; WL, Walker Lane. 10-m National Elevation Data set is from the U.S. Geological Survey.

shear across this zone, based on geologic and geodetic observations [Jayko and Bursik, 2012; Wesnousky et al., 2012; Foy et al., 2012; Bell et al., 2012]. Because the OVF strikes generally clockwise ( $\sim 340^\circ$ ) of local plate boundary motion ( $\sim 323^\circ$ ) [Lifton et al., 2013], the structure accommodates strike-slip motion with an overall releasing geometry (Figure 1) [e.g., Unruh et al., 2014].

The right-oblique OVF comprises numerous predominantly northeast-dipping ( $80 \pm 15^\circ$ ) faults with a subordinate vertical component, typically normal and down to the east (Figure 1) [Beanland and Clark, 1994]. The entirety of the OVF surface trace extends up to  $\sim 140$  km [Slemmons et al., 2008] and coincides with a prominent gap in post-1872 microseismicity [Hough and Hutton, 2008]. The northern and southern boundaries form prominent releasing stepovers that transfer slip to adjacent right-lateral and right-oblique faults near Bishop and Rose Valley (Figure 1) [Slemmons et al., 2008]. The southern terminus of the OVF comprises normal and normal-oblique faults on the northwest margin of the Coso Range extending into Cactus Flat (Figure 1) [Slemmons et al., 2008; Amos et al., 2013a]. Focused extension between the southern OVF and the Little Lake and Airport Lake fault systems (Figure 1) leads to crustal thinning, geothermal activity, and abundant shallow seismicity across the Coso Range [Unruh et al., 2002; Monastero et al., 2002]. The central and northern OVF transfer slip to the White Mountain range front across a relatively broad, diffuse releasing bend with northeast-striking fault splays near Tinemaha Reservoir, Klondike Lake, and Bishop (Figure 1) [e.g., Slemmons et al., 2008]. Overall, the range in previously reported OVF lengths ( $\sim 90$ – $140$  km) [e.g., Carver, 1970; Bryant, 1984a, 1984b, 1988; Beanland and Clark, 1994; Bacon and Pezzopane, 2007; Slemmons et al., 2008] largely stems from uncertainty in the endpoints for past earthquake ruptures.

## 2.2. Geomorphic Setting

The Owens Valley geomorphic surface comprises fluvial and lacustrine deposits fringed by Pleistocene alluvial fans and late Quaternary lava flows. Syntectonic volcanism produced cinder cones and abundant flows contributing to the Big Pine volcanic field dated between  $<0.1$  and  $1.2$  Ma [e.g., Turrin and Gillespie, 1986]. Cosmogenic radionuclide exposure dating of fan deposits in Sierra Nevada piedmont suggests late Pleistocene–Holocene ages between  $\sim 1.2$  and  $124$  ka [Bierman et al., 1995; Zehfuss et al., 2001; Benn et al., 2006; Dühnforth et al., 2007; Le et al., 2007]. Pluvial-lacustrine landforms between the Poverty Hills and Olanca record successive highstands of Owens Lake related to climatic fluctuations throughout the late Pleistocene and Holocene. The modern, dry Owens Lake bottom rests at  $\sim 1084$  m elevation, with dated paleoshorelines corresponding to Marine Isotope Stage (MIS) 2, 6, and possibly 8 mapped at elevations up to  $\sim 1162$ ,  $1170$ ,  $1180$  m, respectively. The approximate age of pluvial-lacustrine features related to reworking of the basin during MIS 2 and 6 highstands are  $\sim 15,870$ – $27,160$  cal yr BP [Koehler and Anderson, 1994; Lubetkin and Clark, 1988; Bacon et al., 2006, 2013, 2014] and  $160 \pm 32$  ka [Jayko and Bacon, 2008], respectively. The equivalent time period for the MIS 8 lake is  $\sim 240$ – $260$  ka [Winograd et al., 2006]. The distribution of progressively older pluvial-lacustrine features at higher elevations indicates a general relationship between surface age and elevation. Fluvial incision, lateral erosion, and aggradation of the Owens River in response to cyclic changes in base level generate suites of fluvial landforms (e.g., terraces and abandoned meanders) along the axis of the Owens Valley [Bacon et al., 2006]. Ongoing evolution of the Owens River meander belt since the MIS 2 highstand produced up to  $\sim 10$  m of local incision, eroding numerous landforms faulted within the past  $\sim 150$  years.

## 2.3. Constraints on Past OVF Earthquakes

The 1872 Owens Valley earthquake is the third largest known historical earthquake in California with comparable displacements and shaking intensities to the 1857 and 1906 San Andreas earthquakes [dePolo et al., 1991; Hough and Hutton, 2008]. Initial investigation of the rupture identified a zone of coseismic deformation, liquefaction, and possible postseismic creep spanning  $\sim 140$  km from Haiwee Reservoir to Bishop Creek, including portions of the Sage Flat fault [Whitney, 1872a, 1872b; Hobbs, 1910; Slemmons et al., 2008]. Detailed mapping described a number of geomorphic and cultural offsets near Lone Pine, with a right-lateral component varying from  $\sim 2$  to  $6$  m (Figures 1 and 2a) [Gilbert, 1884; Hobbs, 1910]. Fault trenching (Figure 2) and scarp measurements across the Lone Pine fault point to three 1872-type earthquakes over the past  $\sim 15$ – $25$  ka, involving repeated dip slip between  $\sim 1$  and  $2$  m [Lubetkin and Clark, 1988; Bacon and Pezzopane, 2007]. Combining this event chronology with three nearby lateral geomorphic offsets measuring  $\sim 6$ ,  $10$ – $12$ , and  $12$ – $18$  m (Figure 2) suggests an average lateral offset of  $4$ – $6$  m [Lubetkin and Clark, 1988]. The maximum right-lateral offset (between  $7$  and  $11$  m) integrates geomorphic offset observations and historical accounts across rupture complexity near Lone Pine (Figure 2a) [Lubetkin and Clark, 1988].

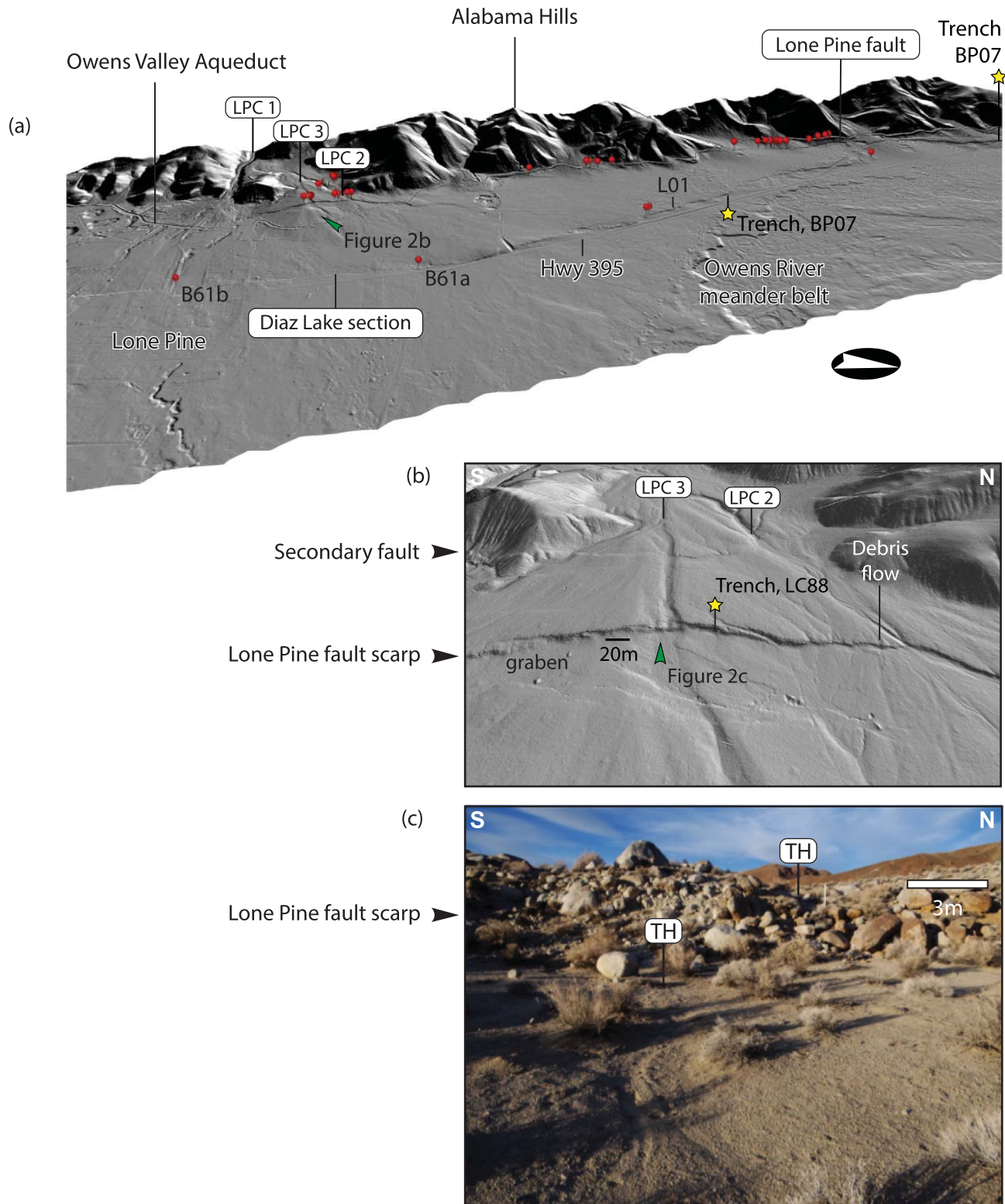


**Figure 2.** Oblique view of hillshade image derived from EarthScope lidar data. (a) View towards the northwest of the Alabama Hills and the southern Owens Valley fault zone, including the Diaz Lake section (east) and the Lone Pine fault (west). Offset features (red markers) include new measurements and sites described in *Bateman* [1961] (B61), *Lubetkin and Clark* [1988] (LC88), and *Bacon and Pezzopane* [2007] (yellow stars, BP07). LPC1, LPC2, and LPC3—Lone Pine Creek 1, 2, and 3. (b) Hillshade image of the faulted Lone Pine fan (Lone Pine, CA) showing right-oblique separation of debris-flow channels and fan axes [*Lubetkin and Clark*, 1988; *Beanland and Clark*, 1994]. (c) View to the west of the offset thalweg (TH) of southern Lone Pine Creek (LPC3) first identified by W. D. Johnson in *Hobbs* [1910].

Identification of 11 additional lateral geomorphic offsets, related mainly to the 1872 earthquake, suggested higher average lateral slip overall ( $6 \pm 2$  m), with a lateral-to-vertical ratio of 6:1 compiled along a relatively short rupture ( $100 \pm 10$  km) [Beanland and Clark, 1994]. Later recognition of comparatively small offsets along the deformed southern margin of Owens Lake [Vittori *et al.*, 1993] and the northeast-striking Red Ridge fault yielded a slightly lower average offset of  $\sim 4.4$  m right-lateral and  $\sim 1.0$  m vertical on a rupture spanning 113–120 km (Figure 1) [McCalpin and Slemmons, 1998; Slemmons *et al.*, 2008]. Initial inspection of the right-lateral component using lidar data suggested significantly lower 1872 slip, averaging  $2.9 \pm 1.0$  m [Madden *et al.*, 2013]. This value does not, however, incorporate historical measurements, previously reported sites, or combined displacements of continuous geomorphic features across subparallel rupture traces.

Although earlier field studies show strong evidence for cumulative displacements predating the 1872 event [Lubetkin and Clark, 1988; Beanland and Clark, 1994], fault trench investigations provide conflicting results on the size and timing of pre-1872 OVF surface ruptures. Near Lone Pine (Figure 2a), widespread rupture characterized by meter-scale vertical separations points to a penultimate event between  $8.8 \pm 0.2$  ka and  $10.2 \pm 0.2$  ka [Bacon and Pezzopane, 2007]. Loose constraints on the antepenultimate event (APE) (between  $\sim 14$  and 24 ka) based on recalculated cosmogenic ages from Bierman *et al.*, [1995] for the Lone Pine alluvial fan ( $17.9 \pm 7.5$  ka) [Bacon and Pezzopane, 2007], liquefied Owens Lake sediments ( $17.5 \pm 1.8$  ka) [Smith and Bischoff, 1997], and rock avalanche debris ( $18.7 \pm 3.9$  ka) [Le *et al.*, 2007] generally agree with long earthquake repeat times over the past  $\sim 25$  ka [Bacon and Pezzopane, 2007]. Trench exposures farther north near Independence (Figure 1), however, indicate a two-event record with  $\sim 15$  cm of dip slip during 1872 and  $\sim 38$  cm during a PE between  $3.3 \pm 0.3$  ka and  $3.8 \pm 0.3$  ka [Lee *et al.*, 2001a]. Different event chronologies for the southern and central OVF potentially suggest more variable strain release patterns over the course of multiple earthquake cycles. Bacon and Pezzopane [2007] relate pre-1872 slip on the central OVF to distributed rupture across a nearby stepover to the southern WMF, possibly correlative with the White Mountain fault MRE estimated at  $\sim 3$  ka (Figure 1) [dePolo, 1989]. In either interpretation, these studies demonstrate recurrence intervals on the order of  $\sim 10^3$ – $10^4$  years for OVF ruptures.

#### 2.4. Fault Slip Rates

OVF slip rate estimates from geologic features averaged over different late Quaternary time intervals contrast by almost an order of magnitude ( $\sim 0.7$ – $4.5$  mm/yr). At the upper end of this range,  $^{36}\text{Cl}$  exposure dating of a basalt flow near Crater Mountain combined with lateral offset of the buried margin ( $235 \pm 15$  m) implies slip at  $\sim 2.8$ – $4.5$  mm/yr since 55–80 ka [Kirby *et al.*, 2008]. In contrast, lower rates typically stem from observations of vertical separations in trench stratigraphy and average lateral-to-vertical slip ratios, yielding slip rates of  $\sim 0.5$ – $2.1$  mm/yr over the past two earthquakes [Lubetkin and Clark, 1988; Beanland and Clark, 1994; Lee *et al.*, 2001a; Zehfuss *et al.*, 2001; Bacon and Pezzopane, 2007]. Although relatively low slip-rate estimates for the Holocene period might reflect the tendency for paleoseismic techniques (e.g., trenching) to underestimate the actual, long-term slip rate [Kirby *et al.*, 2008], the reported range leaves open the possibility of secular variations in slip [e.g., Gold and Cowgill, 2011]. That said, the majority of geologic slip rates fall in general agreement with present-day dextral shear inferred from GPS data at  $2.1 \pm 0.7$  mm/yr [Dixon *et al.*, 2003].

### 3. Methods

#### 3.1. Mapping and Offset Identification

This study relies on lidar data and field mapping to image and analyze displaced landforms intersecting the Owens Valley surface rupture trace. We investigated surface traces of the OVF using the 2007 EarthScope Southern and Eastern California lidar data set accessed from OpenTopography (<http://opentopography.org/>) (Figure 1). From these data, we generated high-resolution (25-cm) bare-earth DEM tiles spanning fault traces using both Triangulated Irregular Network (TIN) and inverse distance weighting (IDW) interpolation methods. We used ESRI ArcGIS to calculate custom slope, hillshade, and contour maps with variable contrast, look, and illumination angles. We also complemented our visualization of the lidar data using National Agricultural Imagery Program digital orthophotography (1-m resolution).

We mapped the fault zone from Cactus Flat in the northwestern Coso Range to Bishop at a scale of 1:1200, focusing on major and secondary fault traces (Figure 1). We provide the resulting linework in supporting information Data Set S1. Based on the overall appearance and fault surface expression, we classified scarps as

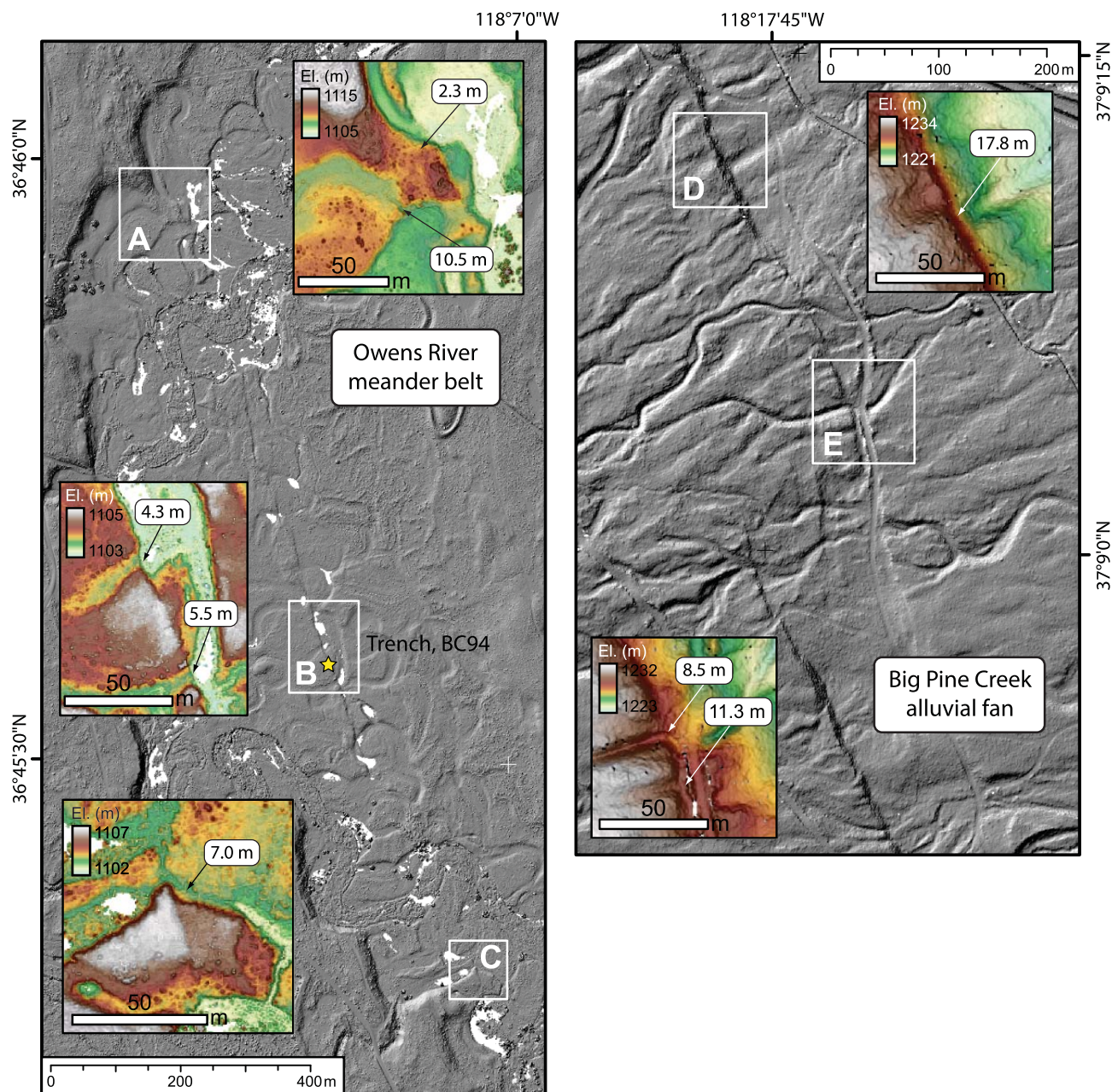


**Figure 3.** Lidar hillshade images of the Owens Valley fault intersecting the Owens River meander belt south of Independence and the Big Pine Creek alluvial fan south of Big Pine (Figure 1). (a–e) Close-ups of custom DEMs (25-cm grid) overlain on slope maps depicting several offset geomorphic features identified and measured by this study. Offset values indicate optimum right-lateral slip determined from EarthScope lidar using LaDiCaoz\_v2 and field study. Yellow star indicates paleoseismic trench site from *Beanland and Clark, [1994] (BC94)*.

certain, approximately located, inferred, or queried. Inspection of the surface rupture at this scale using lidar and imagery enabled us to identify and assess linear to sublinear geomorphic piercing points, as well as evidence for lateral spreading [e.g., *Carver, 1970*]. Examples of ideal landforms for slip measurement include laterally displaced fluvial and debris-flow channels, debris-flow levees, terrace risers, narrow interfluves, lake shorelines, and alluvial fan apices (Figure 3). Our use of naturally variable geomorphic features generally limits us to measuring discrete on-fault deformation and warping within a few tens of meters from fault scarps.

### 3.2. LaDiCaoz\_v2

We used a newly developed software tool, LaDiCaoz\_v2, to measure the lateral and vertical components of slip and estimate associated uncertainties from offset landforms along the OVF. This MATLAB-based GUI for

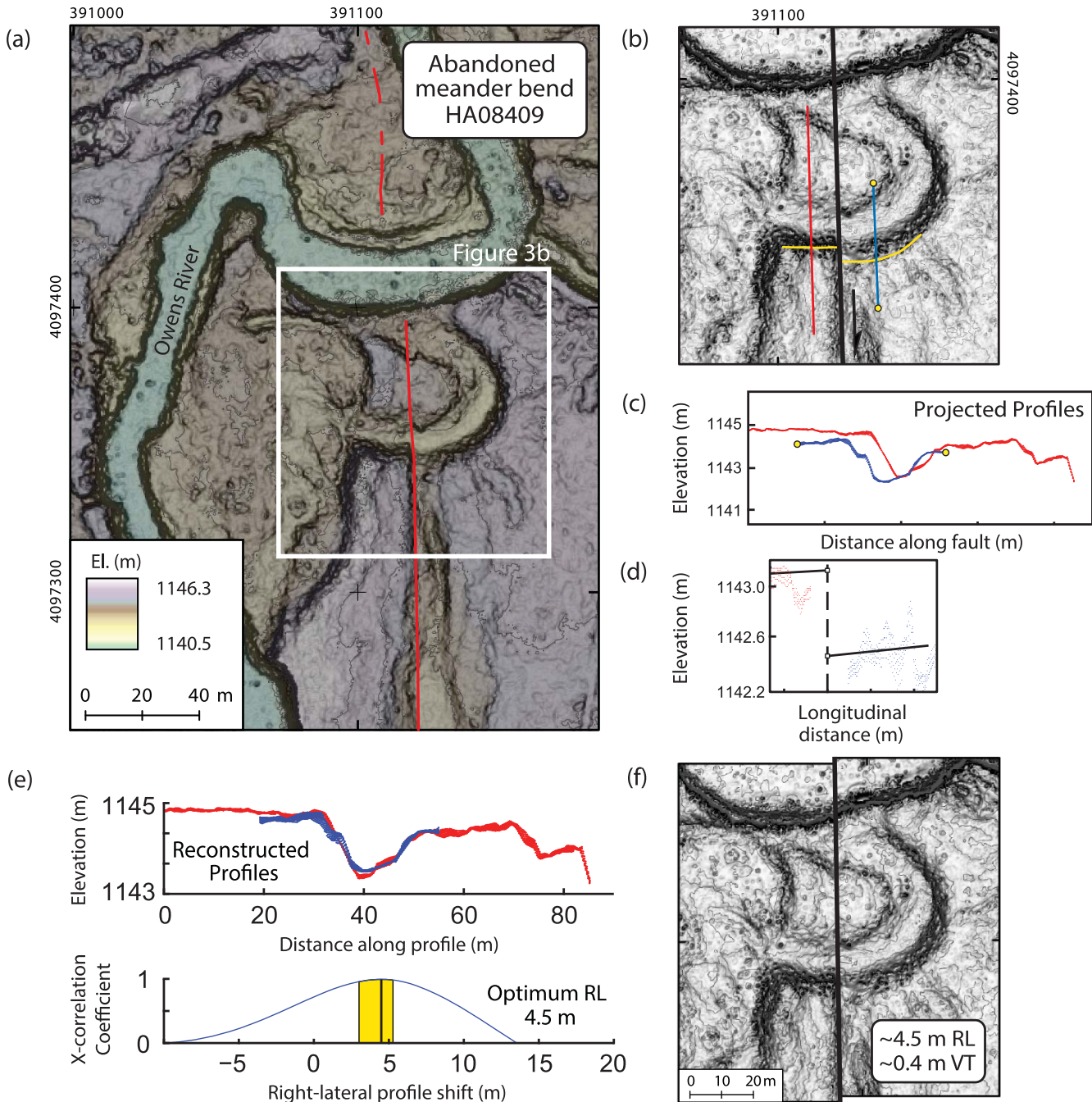


**Figure 4.** Application of the LaDiCaoz\_v2 tool for measuring offset linear geomorphic features. (a) DEM topography draped over a slope map of an abandoned meander bend faulted by the Tinemaha section of the OVF. North of the offset meander, post-1872 incision of the modern Owens River to an elevation of nearly  $\sim 1140$  m conceals the surface rupture trace. (b) Interpreted slope map delineates the general position of the surface trace (black), fault-parallel profile lines on footwall surface (red) and east down hanging wall (blue), and longitudinal tracing (yellow) of the up and down-thrown southern channel margin. (c) Swaths of red and blue elevation points sampled along the corresponding fault-parallel profile lines. (d) Longitudinal cross sections of topographic data extracted in swaths along the landform tracings (yellow lines). Black tracings of the cross section data define the feature slope on the footwall and hanging wall surfaces. (e) Fault-parallel profiles projected onto the fault plane according to the feature slope and shifted by the optimal lateral offset (4.5 m RL) and vertical throw (0.4 m VT). Cross-correlation curve truncated using uncertainty limits determined from back-slipping (indicated by yellow bar). (f) LaDiCaoz\_v2 reconstruction of the geomorphic offset based on DEM topography sliced and back-slipped along the fault trace.

analyzing lidar DEMs is included in supporting information Software S1. LaDiCaoz\_v2 relies on cross-correlation of high-resolution topographic data (Figure 4a) to calculate the displacement of offset geomorphic features related to surface-rupturing earthquakes. This tool produces uniquely shaped PDFs for lateral and vertical offsets, reflecting the distinctiveness of the landform (i.e., the amount of relief, width, and degree of symmetry) relative to the surrounding topography and the displacement amount. The tool also automatically generates a set of output files for additional data analysis and presentation (e.g., kmz and html files with offset measurement values and reconstructions).

LaDiCaoz\_v2 measures displaced geomorphic features based on the cross-correlation of topographic data extracted along two fault-parallel cross-sectional profiles, as follows. First, the user loads an individual lidar DEM into LaDiCaoz\_v2 and traces the fault position and two fault-parallel profile lines across the footwall and hanging wall surfaces (i.e., one on each side of the fault trace) (Figure 4b, black, red, and blue lines, respectively). Swaths of elevation points (usually 0.5 or 1 m wide, but generally a function of DEM resolution) straddling the fault-parallel profile lines are extracted to produce cross-sectional profiles for cross-correlation (Figure 4c). Next, the user traces the length of the geomorphic marker (e.g., ridge crest, channel thalweg, terrace edge) projecting toward the idealized fault plane (Figure 4b, yellow lines) to create longitudinal profile lines (i.e., parallel to the landform) on each side of the fault trace. LaDiCaoz\_v2 uses elevation data extracted along the longitudinal profile lines to generate longitudinal cross sections (Figure 4d). Generalized information from the longitudinal data (the landform's trend and slope) enables the program to project the respective fault-parallel profiles onto a simplified vertical fault plane (Figure 4d, dashed black line). The trend of the geomorphic feature reflects the orientation of the longitudinal tracing in plan view where it intersects the fault (Figure 4b) [Zielke and Arrowsmith, 2012].

LaDiCaoz\_v2 solves for the best-fitting lateral offset using cross-correlation, a sliding dot product that measures the similarity between two waveforms. Cross-correlation is frequently used in signal processing to estimate the shift in time between two known waveforms [Knapp and Carter, 1976]. In this case, the waveforms provided as inputs describe elevation as a function of horizontal distance along the fault. Hence, the final cross-correlation curve (Figure 4e) quantifies the similarity between landforms as a function of lateral separation and mean elevation difference.

LaDiCaoz\_v2 iteratively compares a "key" or template-cropped profile to the complete across-fault topography using along-fault steps, typically equal to the DEM grid spacing (supporting information Figures S1a and S1b). For each lateral offset step, the program determines the difference in mean elevation of key and target (i.e., within the overlapping sections) (supporting information Figure S1c). After subtracting the mean elevation difference (vertical throw) from the key, both profiles are normalized so the area under each curve equals 1, and the dot product is determined (supporting information Figures S1d and S1e). Cross-correlation provides values between  $-1$  and  $1$ , where a value of  $1$  is perfectly correlated (e.g., between same "wave" at same phase) and  $-1$  is perfectly anti-correlated. A value of zero indicates lack of correlation. Repeating this procedure for all possible offset values/increments yields an offset PDF for lateral offset (Figure 4e). The amplitude and wavelength of the lateral offset PDF reflects the similarity of both cross-sectional profiles in consideration of feature trend and slope relative to the fault plane. Because the vertical throw between the projected cross-sectional profiles depends on the horizontal cross-correlation routine, the value is a function of lateral offset.

We visually assessed cross-correlation optima by reconstructing the implicit pre-rupture topography across the fault. LaDiCaoz\_v2 slices and shifts the DEMs along the fault trace, enabling the user to test the result and independently determine the preferred amount of lateral displacement based on "back-slipping" the imagery (Figure 4f). During this step, we also evaluated the plausible offset range for each landform, generally equivalent to a  $2\sigma$  standard deviation for a Gaussian PDF. Our reported offset ranges, however, are frequently asymmetrical about the optimum value. Restoration of landforms with two or more piercing points, such as debris-flow channels, yields a range of values often predicted by the overall width of the landform. For example, restoration of the channel margin impeding downstream flow often provides a minimum value, whereas the sheltered margin usually yields a maximum [Cowgill, 2007]. We truncated each cross-correlation curve in accordance with the permissible range from back-slipping, thus producing a unique displacement PDF for each landform (Figure 4e).

The range of offset values from visual inspection may not account for assumptions related to the position of the fault plane on the scarp face. Because the fault plane is generally concealed outside of trench exposures,

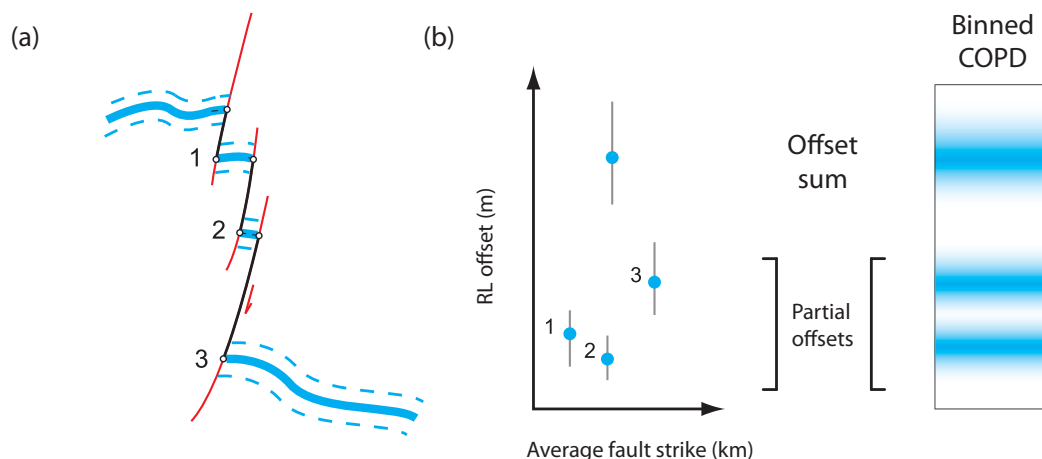


**Figure 5.** (a) Schematic illustration of summing approach for features offset across multiple discrete faults. (b) Individual offset measurements represent partial slip with uncertainty ranges provided by back-slipping. Multiple partial slip measurements contribute to an offset sum with associated uncertainties determined using a Monte Carlo routine. The lower distributions in the binned COPD plot reflect stacked values of partial offset, whereas the uppermost distribution is the sum of the partial offset distribution. The sum is equal to the estimated net offset and contributes to COPD plots binned along strike.

we systematically plot the fault near its expected intersection with the surface, between one-third to one-half the total scarp height [e.g., *Thompson et al.*, 2002]. Additional variability may result from changes in fault dip, multiple surface ruptures, and post-earthquake incision and degradation of the scarp. Compared to simple scarp profiles, however, LaDiCaoz\_v2 provides an advantageous approach to determining vertical offset, because the measurement spans the laterally displaced landform and accounts for the landform slope.

Similar to previous lidar and field-based studies of lateral geomorphic offset, we assigned a confidence rating to each measurement (supporting information Table S1) [e.g., *Sieh*, 1978]. Whereas measurement uncertainties place bounds on the permissible range of separations, confidence ratings quantify the authenticity of apparent offsets and the reliability of reconstructions [e.g., *Scharer et al.*, 2014]. As such, we do not conflate uncertainty with confidence. We modified criteria developed by *Sieh* [1978] and *Lienkaemper* [2001] to include a local calibration for Owens Valley landforms. Our confidence ranges from high (5), moderate-high (4), moderate (3), moderate-low (2), to low (1) based on feature distinctiveness, complexity of the fault trace, relative obliquity of features, degree of modification or erosion, and quality of the lidar DEM for that site (supporting information Table S1).

We treat multiple offsets of an individual geomorphic marker across closely spaced subparallel fault segments by summing to find the cumulative value (Figure 5) [e.g., *McGill and Rubin*, 1999]. This approach is advantageous because we do not know the chronology of individual earthquakes contributing to such displacements. We only correlate and sum partial offsets measured for the same landform, because different landforms offset within a zone of faulting likely reflect contrasting surface ages. Summed measurements occur within zones of deformation between ~5 and 90 m wide. In order to preserve the distribution of the measured uncertainty, we add triangular PDFs following a Monte Carlo approach. In each calculation, the Monte Carlo simulation samples PDFs associated with each measurement over 10,000 trials to generate an offset histogram [e.g., *Amos et al.*, 2010]. Reported values reflect the mode and corresponding 95% confidence intervals.

### 3.3. Field Verification

We field visited the majority of our offset sites identified in the lidar data and those reported by previous studies to calibrate our confidence ratings and verify our measurements. We used hillshade and contour base maps loaded onto an Apple iPad running GIS Pro version 3 to locate each offset and traverse the surface rupture. Documentation for sites with confidence of two and above (see Offset Observations in supporting information Text S1) includes systematic mapping, offset measurements, photographs of the local conditions (e.g., Figure 6), and descriptions of key geomorphic and geologic relationships, including the continuity of geomorphic features, impacts of subsequent erosion and sedimentation, scarp slope angle,

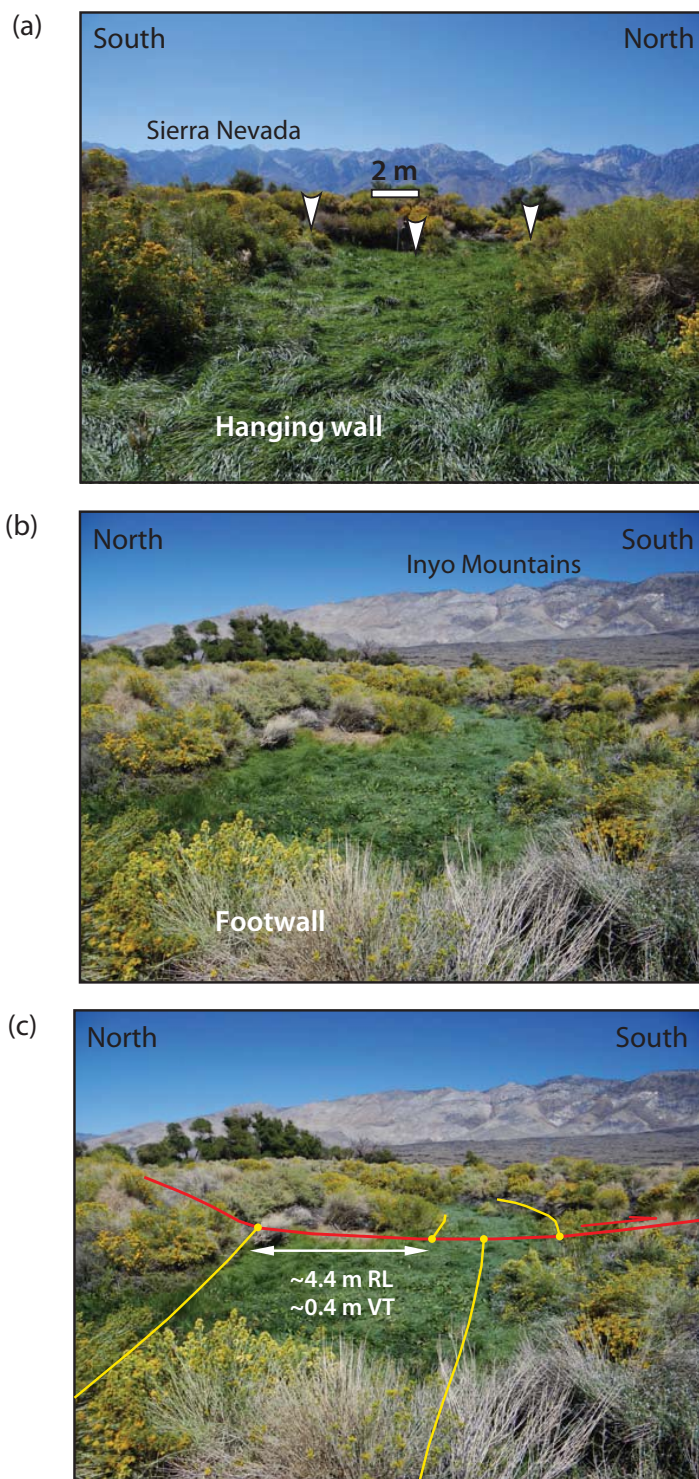


**Figure 6.** Example of a high confidence geomorphic offset documented in the field (see Figure 4 for map view). (a) View from the hanging wall to the west down-channel and normal to the OVF. White arrows mark the intersection of the OVF with the thalweg and channel margins. (b) Uninterpreted view from the footwall up-channel and to the east toward the hanging wall. (c) Offset values (~4.4 m right-lateral, 0.4 m east-down vertical) rely on field measurement of channel margins (traced in yellow) and bounding tread surface to the north. The Tinemaha section of the OVF is mapped in red. RL, right-lateral; VT, vertical throw.

apparent relative ages of foot-wall and hanging wall features, fault zone width, and the presence of human modification.

### 3.4. Reconstruction of OVF Earthquakes

We assessed the distribution of surface slip for past earthquake surface ruptures following the approach established by *McGill and Sieh* [1991] and recently expanded by *Zielke et al.* [2012]. Typically, such studies rely on histograms [*Wallace*, 1968] and cumulative offset probability distributions (COPDs) [*McGill and Sieh*, 1991] to assign successive peaks or clusters of lateral offset to individual earthquakes. Peaks in the COPD may reflect single-event or cumulative slip due to multiple surface-rupturing earthquakes, following two primary assumptions: (1) climatic events generate and preserve sufficient populations of geomorphic markers to effectively record each rupture [*Sieh*, 1978], and (2) geomorphic separations reflect coseismic slip in the absence of aseismic creep [*McGill and Sieh*, 1991]. Provided that peaks in the COPD correspond to frequent values of surface slip during past large earthquakes, displacement during the MRE typically contributes to the group of smallest measured offsets, represented by the first strong peak. Subsequent peaks in the COPD reflect cumulative slip, with each group encompassing an increasing number of past earthquakes. Because cumulative offsets are generally less well preserved in the landscape [e.g., *Weldon et al.*, 1996], multiple-event COPDs generally display a strong peak associated with the MRE and a tail of subsidiary peaks at decaying heights related to cumulative displacements [e.g., *Klinger et al.*, 2011].

Although the total breadth of an individual COPD peak may in part reflect measurement uncertainty [e.g., Gold *et al.*, 2013], actual along-strike differences in surface slip during individual surface-rupturing earthquakes are present at number of spatial length scales (sub-kilometer to tens of kilometers). Potential contributing factors include the influence of fault geometry [e.g., Sieh *et al.*, 1993; Zacharisen and Sieh, 1995; Treiman *et al.*, 2002; Klinger *et al.*, 2006; Fletcher *et al.*, 2014; Teran *et al.*, 2015]; the presence of distributed shear, warping, or rotation [McGill and Rubin, 1999; Rockwell *et al.*, 2002; Cochran *et al.*, 2009; Oskin *et al.*, 2012; Milliner *et al.*, 2015; Gold *et al.*, 2015]; and heterogeneously distributed mechanical properties (e.g., fault strength and asperities) along the fault [e.g., Mendoza, 1993; Ozacar and Beck, 2004; Rockwell and Klinger, 2013; Chen *et al.*, 2015]. As a result, closely spaced complex peaks in the along-strike COPD may reflect inherent variability in surface slip during a single event, as well as the influence of multiple overlapping ruptures [e.g., McGill and Rubin, 1999; Madden *et al.*, 2013].

Because the 1872 surface rupture spanned a number of subparallel fault traces [e.g., Carver, 1970], we analyzed geomorphic offsets along individual sections of the OVF using separate COPDs of lateral and vertical offset (supporting information Figures S2–S12). These COPDs incorporate summed LaDiCaoz\_v2 measurements (Figure 5) and previously reported features. We assigned nominal uncertainties of 20% to measurements lacking error estimates based on historical reports and fault trench analyses. Fault sections typically span ~5–20 km in length and are defined based on changes in fault strike, relays, or stepovers [e.g., Bryant, 1984a, 1984b, 1988; Beanland and Clark, 1994; Slemmons *et al.*, 2008]. This approach reduces the influence of along-strike complexities, providing a simplified view useful for assessing evidence of heterogeneous surface slip during individual faulting events.

Our reconstructed slip distributions for the entire fault follow the binned COPD approach of Zielke *et al.* [2012]. These COPD plots incorporate only moderate to high confidence measurements (confidence ratings 3–5) averaged or binned along discrete fault lengths (typically 2–5 km increments). We correlated offset groups for adjoining bins along strike based on peak amplitude and spacing [e.g., McGill and Sieh, 1991; Klinger *et al.*, 2011]. Where multimodal peaks in the binned COPD occur, we delineated slip curves using mean values for contributing measurements rather than selecting the highest probability bins [e.g., Zielke *et al.*, 2012]. Although event classifications are nonunique, our slip distributions represent a preferred solution in consideration of all available data.

One primary result of our analysis along the OVF is an average estimate of slip-per-event, which we calculated using three methods. First, we averaged offset values for each fault section length and combined these values using factors that normalize average offset with respect to the total rupture length. Second, we used this method to provide average displacement values, which we derived based on the assumption that the OVF dips an average of  $80 \pm 15^\circ$  east [Beanland and Clark, 1994]. Lastly, for the 1872 Owens Valley earthquake, we averaged displacements summed across overlapping faults that ruptured in 1872 (see section 5.2 for additional discussion). The result is an estimate of net average displacement for the 1872 earthquake. We compiled averages of the vertical component for past throughgoing ruptures based on throw measured across these lateral features. All errors reported for averages in peak lateral and vertical offset reflect the  $2\sigma$  standard deviation.

## 4. Results

### 4.1. Offset Observations

Our comprehensive database of displaced geomorphic features for the OVF incorporates newly identified landforms, remeasured features described in earlier field studies [Hobbs, 1910; Lubetkin and Clark, 1988; Beanland and Clark, 1994; Slemmons *et al.*, 2008], and published field values for sites we were not able to remeasure (supporting information Text S1). Previously reported measurements include features affected by cultural or geomorphic modification in the decades following earthquake rupture [Bateman, 1961], as well as data based on trench excavations, scarp profiles, and geophysical methods [Lubetkin and Clark, 1988; Zehfuss *et al.*, 2001; Lee *et al.*, 2001a; Bacon and Pezzopane, 2007; Kirby *et al.*, 2008]. Supporting information Table S2 catalogs offset features including field, LaDiCaoz\_v2, and back-slip values. Our database is also available as an ArcGIS shape file and a Google Earth kmz file, containing site descriptions and imagery based on lidar DEMs (supporting information Data Sets S2 and S3). LaDiCaoz\_v2 exports these images during each offset reconstruction. Html files summarize the details of each restoration, showing the current

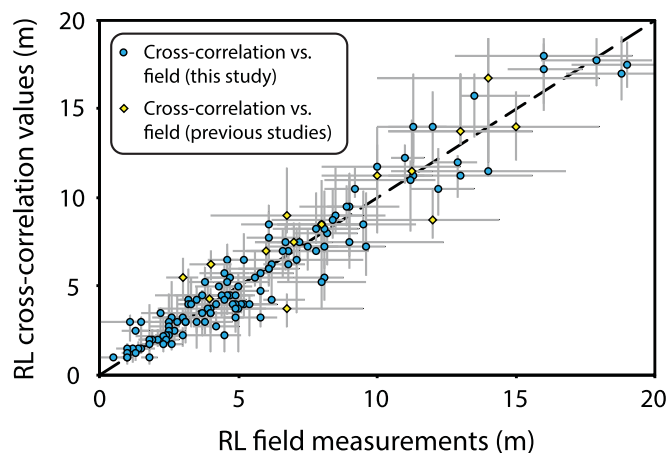


**Figure 7.** Comparison between lateral offsets measured using LaDiCaoz\_v2 and in the field (blue points) and previously published studies (yellow diamonds). Dashed black line indicates a 1:1 relationship. Uncertainties for lidar measurements reflect limits determined from back-slipping, whereas field values include errors evaluated on-site.

and back-slipped topography and corresponding cross-correlation curves for each site (supporting information Data Set S4). Supporting information Table S3 catalogs information from previously published sources on measurements gathered in the field from offsets we did not revisit as part of this study.

Our complementary field observations at 154 sites compare well with lateral offsets measured using LaDiCaoz\_v2, indicating a nearly 1:1 fit with a slope of 0.99 and a correlation coefficient of 0.93 (Figure 7). Similarly, our lidar measurements compare favorably with sites originally documented by *Lubetkin and Clark* [1988], *Vittori et al.* [1993], *Beanland and Clark* [1994], and *Slemmons et al.*

[2008], yielding a slope 0.95 and a correlation coefficient of 0.98. We note several factors that may hinder field efforts to accurately project sublinear features toward the fault plane, however, including significant tilting, warping, or distributed faulting. Lidar analysis generally permits greater control when establishing linear trends and projecting piercing lines across scarps with significant vertical separation.

We compile right-lateral and vertical offset as a function of distance along the average OVF strike ( $340^\circ$ ) to investigate along-fault patterns in surface slip (Figure 8). Lateral offsets vary from  $\sim 1.0$  up to 87.3 m and demonstrate vertical offset between  $\sim 0.1$  and 24.1 m. Our measurements show an overall positive correlation between throw and lateral offset (Figure 9). Histograms and COPD plots for the entire fault and for major fault sections (northern, central, and southern) reveal multiple subsidiary peaks in the distribution of surface slip (Figure 10). Similarly, binned COPD plots across overlapping strands highlight complexities masking the shape of slip distributions for past OVF earthquakes (Figure 11). Thus, we divide measurements by individual fault section (e.g., Figure 8a) for subsequent analysis (see supporting information Text S1 for additional explanation). The resulting scatterplots, histograms, and COPD plots (supporting information Figures S2–S12) enable us to systematically classify single and multiple-event offset measurements for individual sections. Our reconstructions for 1872 and earlier earthquakes build on observations for individual sections and delineate separate slip curves based on binned COPD plots for the main OVF trace (Figure 11d) and the subsidiary Lone Pine fault (Figure 11e). Reported averages for past earthquakes incorporate only measurements rated moderate to high in confidence.

#### 4.2. 1872 Earthquake

Our reconstruction of the historical 1872 earthquake demonstrates the overall magnitude and extent of surface slip during this event. We attribute 78 laterally displaced landforms and relatively fresh scarps spanning at least  $\sim 113$  km of the OVF to slip during this surface rupture (Figure 11) [Slemmons et al., 2008]. This length confirms our preferred southern terminus based on lidar mapping, which coincides roughly with the oblique and northeast-striking Red Ridge fault [Slemmons et al., 2008] (Figure 1). Likewise, we tentatively terminate the 1872 rupture between Klondike Lake and Bishop (Figure 11a), although relatively fresh scarps and lineaments demonstrate some uncertainty in the distributed nature of 1872 slip at the northern terminus. Scarps resembling possible rupture into Bishop (e.g., *Hobbs* [1910]) are beyond the extent of the airborne lidar data (Figure 1) and cannot be definitively attributed to offset in 1872 (supporting information Data Set S1).

Figure 12 shows a linear interpolation of lateral and vertical offsets along strike as a means to visually assess distributed slip along fault sections involved in the 1872 rupture trace. Individual lateral offset measurements depicted vary from  $1.0 \pm 0.2$  m to  $5.5 + 1.1/-1.3$  m along strike, possibly reaching  $6.0 + 1.9/-1.6$  m,

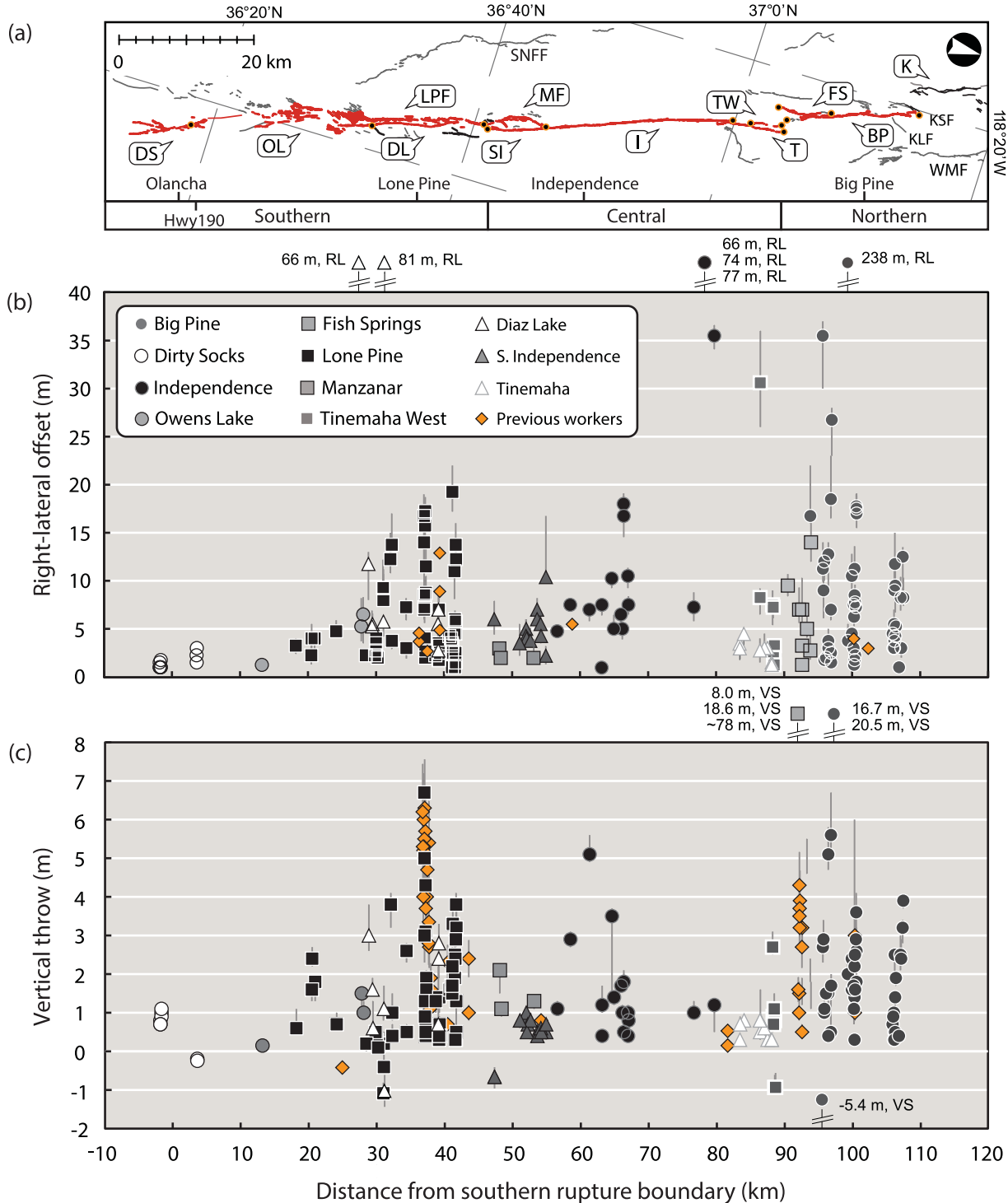


**Figure 8.** Compilation of small geomorphic offsets measured from lidar using LaDiCaoz\_v2 along average OVF strike (340°) (supporting information Tables S2 and S3). Data include confidence ratings of low-moderate to high and omit net values determined by summing. Gray error bars show uncertainty limits determined visually from back-slipping. (a) The spatial distribution of OVF scarps (red lines) mapped from EarthScope lidar and classified by Owens Valley fault section (orange and black points), following previous mapping by *Beanland and Clark* [1994], *Bryant* [1984a, 1984b], and *Slemmons et al.* [2008]. Nearby faults are taken from the U.S. Geological Survey Quaternary fault and fold database. From south to north: DS, Dirty Socks; OL, Owens Lake; LP, Lone Pine fault; DL, Diaz Lake; IS, southern Independence; MF, Manzanar fault; I, Independence; T, Tinemaha; TW, western Tinemaha; FS, Fish Springs; BP, Big Pine; K, Keough section of Sierra Nevada frontal fault (SNNF), KLF, Klondike Lake fault; KSF, Klondike Springs fault; WMF, White Mountain fault. (b) Right-lateral offset measurements symbolized by fault section include previously reported values (orange diamonds) from *Bateman* [1961], *Lubetkin and Clark* [1988], *Beanland and Clark* [1994], *Lee et al.* [2001a], *Zehfuss et al.* [2001], and *Slemmons et al.* [2008]. (c) Along-strike compilation of measured vertical throw. Throw is predominantly east-down, with negative values indicative of downward motion to the west.

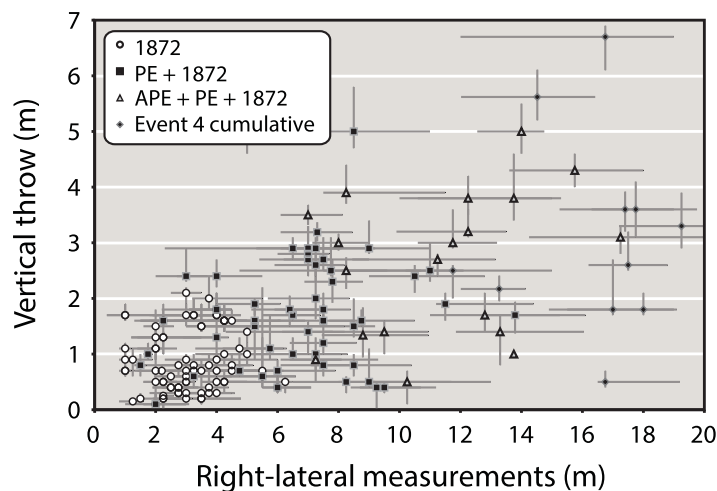


**Figure 9.** Vertical fault throw plotted as a function of right-lateral offset. Individual measurements assigned to single-event and cumulative earthquakes indicate predictions based on binned COPD plots (see Figure 11). Gray error bars reflect the range of uncertainty provided by back-slipping of lidar images in LaDiCaoz\_v2.

Crater Mountain (Figure 12b; Site HA09938f in supporting information Table S2). Supporting information Figure S13 shows right-lateral and vertical measurements related to 1872 projected onto a simplified fault plane ( $340^\circ$  strike) and demonstrates the relative variability in the vertical component measured along strike.

The average lateral offset for landforms affected by the 1872 earthquake is  $3.3 \pm 1.1$  m (supporting information Table S4), corresponding to an average vertical of  $0.8 \pm 0.5$  m based on throw across these features. These values represent the average 1872 lateral and vertical offset one might expect to find at any particular location along of the rupture. Where both components of surface slip are moderate to high in confidence at a given site, we calculate a site-specific ratio of lateral-to-vertical offset. Figure 12c shows an interpolation of these ratios along strike, and averages for individual fault sections indicate a ratio of  $\sim 6:1$  overall. This site-based approach to calculating the slip ratio yields relatively unbiased values in comparison with ratios determined by dividing the average lateral by the average vertical offset ( $\sim 3:1$ , in this case). This lower ratio does not convey the actual variability observed between the two slip components (Figure 12c).

#### 4.3. Prehistoric Earthquakes

Our along-strike compilation of displaced landforms also provides evidence for at least two pre-1872 earthquakes on the OVF. While these earthquakes produce fairly subtle, low-amplitude peaks in the net COPD (Figure 10b), cumulative peaks in the along-strike binned COPD plots appear relatively distinct (Figure 11 and supporting information Figures S2–S12). We document cumulative offsets mainly along the northern and southern OVF (Figures 9 and 10). In northern Owens Valley, active fault traces deform surficial Crater Mountain basalt flows dated between  $\sim 55$  and 80 ka [e.g., Kirby *et al.*, 2008] and late Pleistocene–Holocene Big Pine alluvial fan surfaces likely correlative with debris flows in the Sierra Nevada piedmont dated  $33.5 \pm 4.1$  ka and younger [Dühnforth *et al.*, 2007] (Figure 11). In central Owens Valley, possible cumulative offsets occupy fluvial and lacustrine surfaces at elevations above  $\sim 1120$  m, with likely ages of  $\sim 7700$  cal yr BP or older [Bacon *et al.*, 2006]. PE and older offsets along Lone Pine fault traces mainly occur on fan surfaces comprising debris flows dated  $25.4 \pm 6.0$  ka and younger [Bierman *et al.*, 1995].

We attribute 50 individual lateral offsets to possible cumulative slip during the most recent 1872 event and the PE (Figure 11 and supporting information Figure S13). Cumulative right-lateral and vertical throw average  $7.1 \pm 2.0$  m and  $1.6 \pm 0.9$  m, respectively (supporting information Table S4). Right-lateral slip reaches local maxima along the LPF ( $8.5 + 2.5/-1.0$  m, Site HA03704f in supporting information Table S2) and northern Big Pine section ( $9.5 + 2.8/-1.9$  m, Site HA10633d in supporting information Table S2). Resolving these measurements on an average  $80^\circ$  dipping fault plane suggests a mean cumulative displacement of  $7.3 \pm 2.0$  m (supporting information Figure S13c) and PE slip roughly comparable to the 1872 event on the southern and northern fault sections. Displaced landforms contributing to the PE peak in the along-strike

with a section of maximum slip near Independence (Figure 12a; HA05417f and HA05661a in supporting information Table S2). Possible 1872 outliers along the central OVF may record higher lateral slip approaching  $\sim 7$  m (e.g., Sites HA04735e and HA05366c,d), although the presence of smaller adjacent lateral offsets support the interpretation of these offsets as cumulative. Throw measurements across these features vary up to  $\sim 2.0 + 0.4/-0.1$  m at the thalweg of LPC3 on the Lone Pine fan (Figure 2) [e.g., Lubetkin and Clark, 1988; Beanland and Clark, 1994] and possibly  $2.0 + 0.4/-0.2$  m on the northern flank of

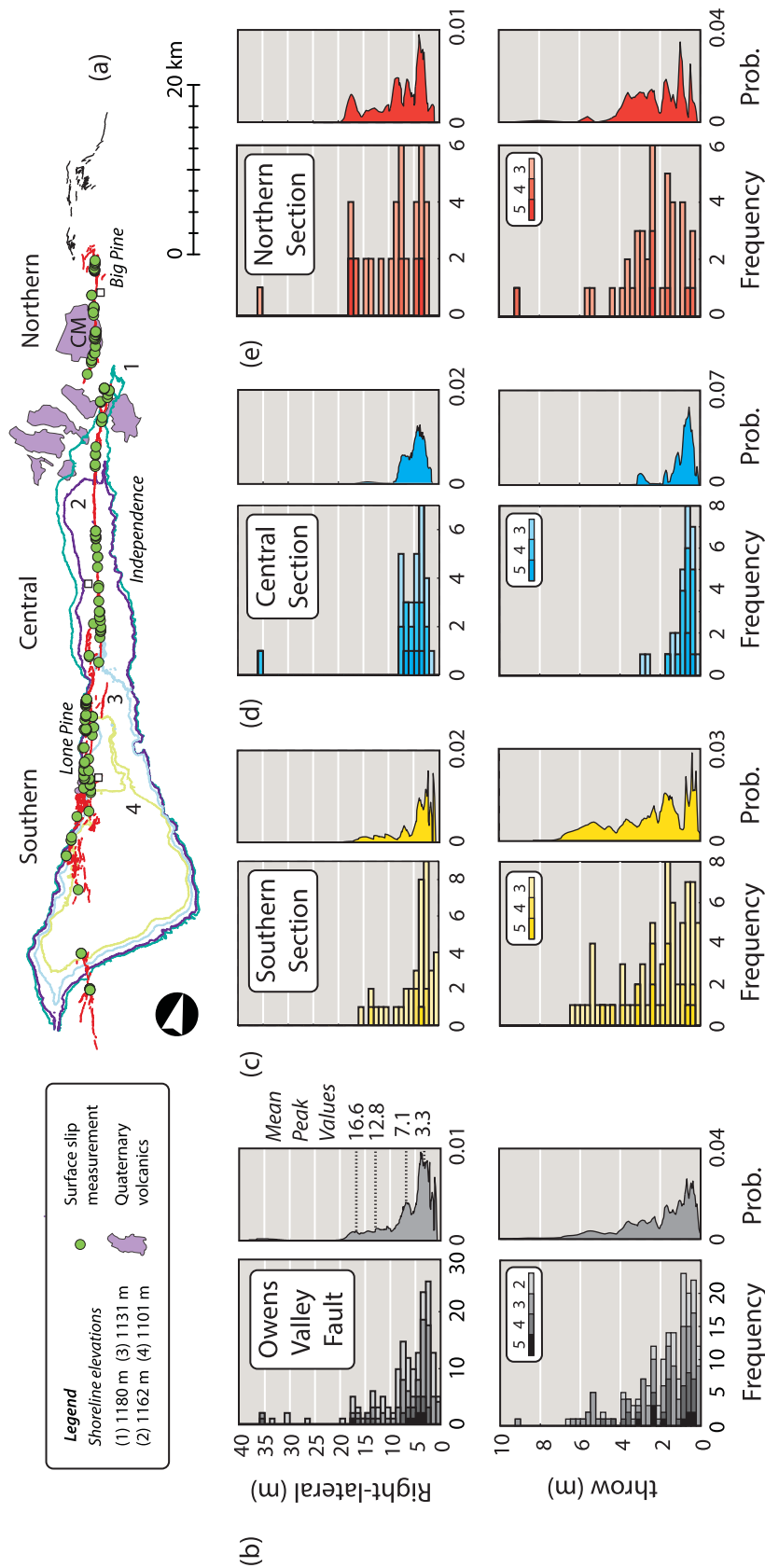


**Figure 10.** Frequency distributions and cumulative offset probability density (COPD) plots for lateral and vertical offsets, compiled using bin sizes of 1 and 0.25 m, respectively (supporting information Tables S2 and S3). Histograms omit uncertainties, whereas COPD plots incorporate PDFs generated by the cross-correlation routine and truncated based on the range of uncertainty from back-slipping. Data are color-coded according to major sections of the OVF. (a) Scarps along the southern, central, and northern sections of the OVF relative to volcanic flows (purple) and a few representative elevation contours, generally corresponding to recognized pluvial-lacustrine features (#1–4) [Bacon et al., 2006; Jayko and Bacon, 2008; Bacon et al., 2013; Bacon et al., 2014]. Age estimates for features documented near (1) 1180 m, (2) 1162 m, (3) 1131 m, and (4) 1101 m are  $160 \pm 32$  ka [Jayko and Bacon, 2008],  $23,230\text{--}26,250$  cal yr BP [Bacon et al., 2006],  $15,870\text{--}16,230$  cal yr BP [Bacon et al., 2014], and  $300 \pm 30$  to  $400 \pm 30$  yr BP [Bacon et al., 2013], respectively. Green points mark surface slip measurements based on geomorphic features. CM, Crater Mountain. Volcanic flows are from the California Geological Survey. (b–e) Optimum offset values for the southern (yellow), central (blue), and northern (red) sections are grouped and shaded by confidence rating. COPD plots use moderate to high confidence offsets and incorporate summed values.

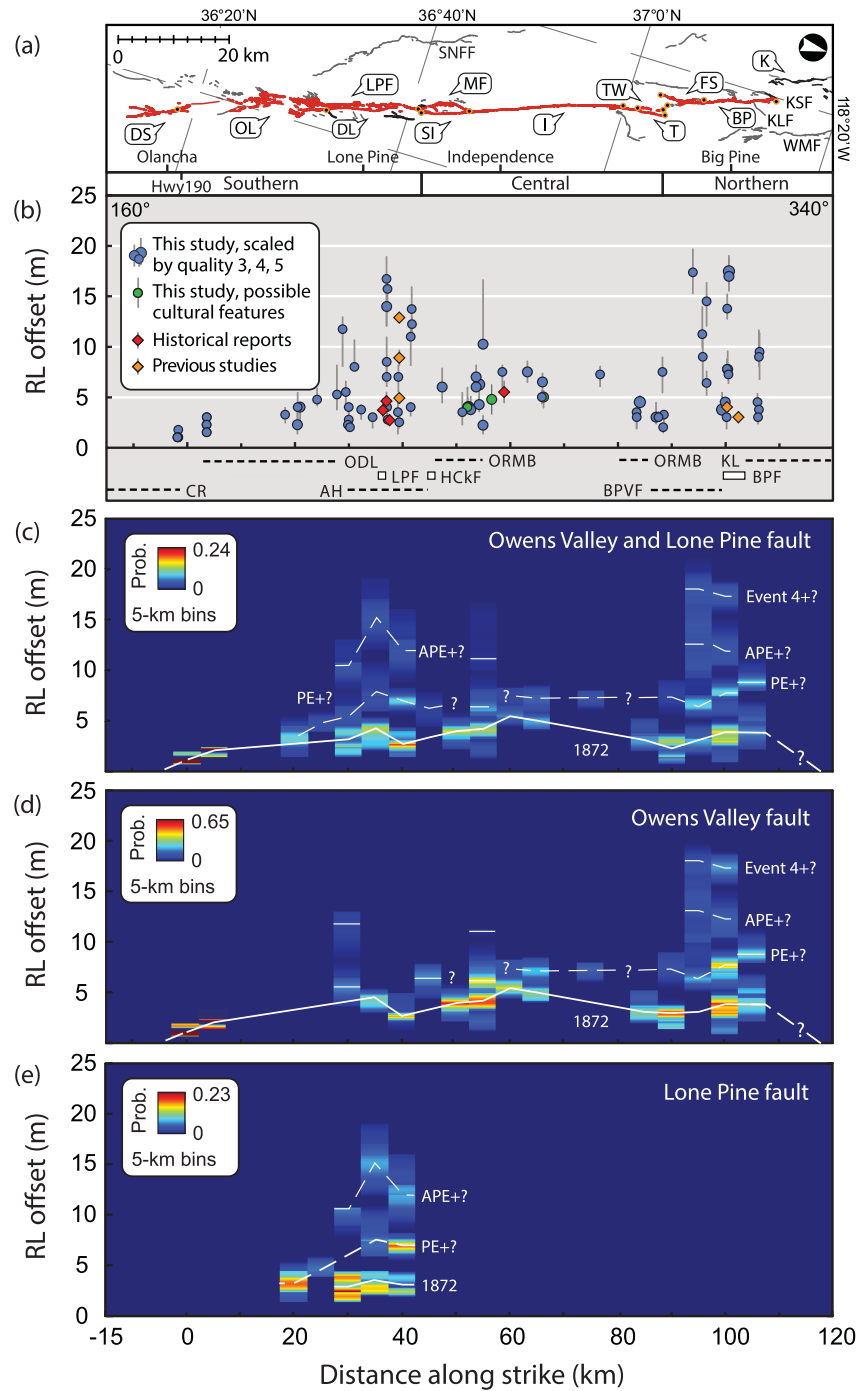


**Figure 11.** Possible surface slip reconstructions for past large Owens Valley fault earthquakes derived from binned COPD plots. PE, penultimate event; APE, antepenultimate event. (a) Scarps mapped from EarthScope lidar with fault section abbreviations similar to Figure 8a. (b) Right-lateral offset measurements scaled by confidence rating, including historic measurements (red points) summarized in *Bateman* [1961], possible cultural features (green points), and previously reported values (orange diamonds) [Lee *et al.*, 2001a]. Grey bars reflect the range of uncertainty previously reported or provided by back-slipping. Lower scale bar describes the along-strike spatial extent of key geologic and geomorphic features. From south to north: CR, Coso Range; ODL, Owens dry lake; AH, Alabama Hills; LPF, Lone Pine fan; HCKF, Hogback Creek fan; BPVF, Big Pine volcanic field; ORMB, Owens River meander belt; KL, Klondike Lake; BPF, Big Pine fan. (c) 5-km binned COPD plot calculated along strike for data ranked moderate and higher in confidence. Warmer values correspond to peaks in distributed offset probability. (d-e) Additional binned COPDs depict the distribution of surface slip measurements compiled along main traces of the OVF and the Lone Pine fault in southern Owens Valley.

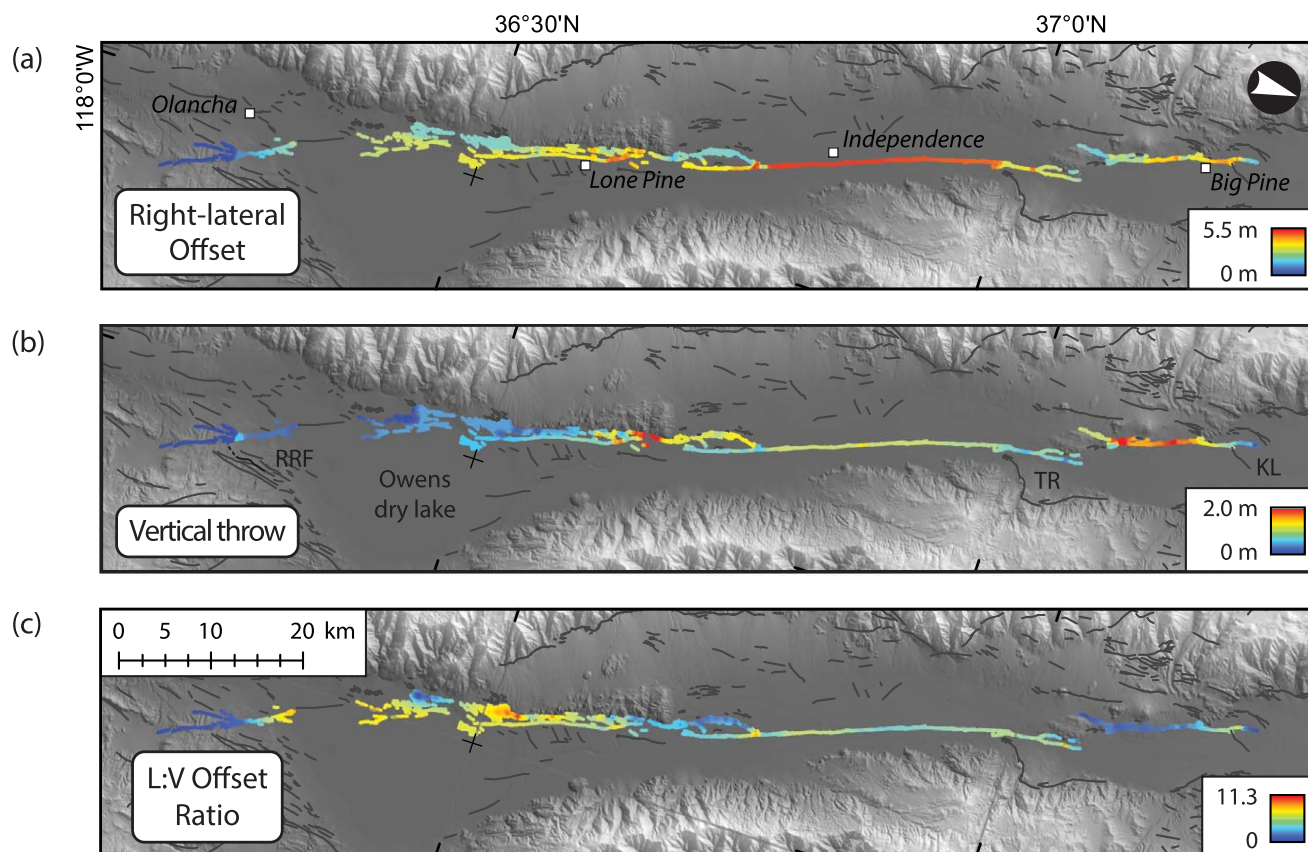


**Figure 12.** Slip distributions for the 1872 Owens Valley surface rupture interpolated from offset measurements compiled along strike (e.g., Figure 11). (a) Right-lateral measurements and summed offset values show the distribution of lateral slip without uncertainties. (b) Distribution of vertical throw following the same approach. (c) Lateral-to-vertical (L:V) offset ratios calculated at sites where both measurements rank moderate in confidence or higher. Active faults from the U.S. Geological Survey Quaternary fault and fold database appear gray and drape a hillshade image combined with 10-m National Elevation Data from the U.S. Geological Survey. Features abbreviated, from south to north: RRF, Red Ridge fault; TR, Tinemaha Reservoir; KL, Klondike Lake.

binned COPD occur along a similar rupture extent to the 1872 event (Figure 11). Notably, vertical offsets related to past ruptures generate a multimodal distribution in vertical COPD plots (Figure 9), perhaps indicating greater variability in the along-strike vertical component relative to the lateral component (Figure 12 and supporting information Figure S13).

Additional larger-offset groups apparent in the binned COPD broadly resemble earlier Owens Valley earthquakes (Figure 11). Although subtle peaks encompass a number of relatively robust lateral offsets in the along-fault COPD, these observations are considerably sparser than offsets contributing to the 1872 and PE ruptures (Figures 10 and 11). Cumulative offsets possibly reflecting lateral slip in the APE include 17 measurements, varying from  $\sim 7.2$  to 16.5 m, with average lateral and vertical offset of  $12.8 \pm 1.5$  m and  $3.2 \pm 0.9$  m, respectively (supporting information Figure S13 and Table S4). A fourth group of landforms encompasses nine cumulative offsets between 11.7 and 18.0 m, with a mean of  $16.6 \pm 1.4$  m. Mean cumulative displacements for the possible APE and fourth event equal  $13.2 \pm 1.6$  m and  $16.7 \pm 1.5$  m, respectively (supporting information Figure S13c).

Despite the longer-term record presented by large offsets, most landforms intersecting the Independence and Diaz Lake sections preserve mainly 1872 surface slip (Figure 8). As a result, reconstructions of the PE and APE across the central OVF are less certain (Figure 11). The limited geomorphic record along the valley axis is a natural consequence of erosion and deposition associated with the  $\sim 25$  ka Owens Lake highstand (Figure 10a) [Bacon *et al.*, 2014], subsequent incision, development of the Owens River floodplains, and ongoing eolian processes. The significant reworking of surfaces across much of the valley floor did not completely remove all cumulative lateral offsets (e.g., [Beanland and Clark, 1994]), and we document

several relatively large-magnitude apparent lateral offsets between  $\sim 35$  and 87 m, presumably developed over the course of many seismic cycles (Figure 8b and supporting information Table S2). Most of these landforms stand in relief above the younger Owens River floodplain surfaces and include relatively subtle relict fluvial channels, terraces, fans, and the margins of an offset basin (supporting information Text S1).

## 5. Discussion

### 5.1. Implications for Geomorphic Offset Compilations

Our analysis of geomorphic offsets along the OVF illuminates several key issues that should be considered by similar studies along active strike-slip faults. First, the millennial return period for large OVF earthquakes [Lubetkin and Clark, 1988; Beanland and Clark, 1994; Bierman et al., 1995; Lee et al., 2001a; Bacon and Pezzopane, 2007] increases the likelihood that the rate of landform development in the Owens Valley outpaces the rate of fault slip and earthquake recurrence. Despite the arid Owens Valley climate, evidence for erosion and modification of the 1872 surface rupture trace suggests that the time between successive large earthquakes ( $\sim 3$ –10 ka) is likely sufficient to form fluvial and debris-flow channels, terrace risers, and other geomorphic features useful for reconstructions of surface slip. This combination of a relatively modest fault slip rate in a geomorphically active environment potentially offers a more continuous record of surface-rupturing earthquakes compared with faster slipping plate boundary faults. For example, similar return periods for landscape formation and earthquakes along the San Andreas lead to ambiguity in interpreting single peaks in a COPD as individual or cumulative events [e.g., Ludwig et al., 2010; Zielke et al., 2010]. An obvious trade-off for faults with longer earthquake return periods like the OVF, however, is the prevalence of relatively young surfaces, which record relatively few past surface ruptures [e.g., Slemmons et al., 2008]. Geomorphic decay also reduces the fidelity of older, cumulative offsets, masking the signal of prehistoric surface ruptures [e.g., Klinger et al., 2011]. Such decay is evident in our data set as lower cumulative offset peaks in COPD plots for higher offset values (Figure 10). As a consequence, definitive correlations between cumulative peaks depicted in binned COPD plots would be substantially strengthened by further subsurface trenching investigations.

Second, our study demonstrates the importance of verifying offsets in the field and analyzing COPDs for individual fault sections along surface ruptures with significant geometric segmentation. Although a component of the uncertainty associated with each COPD peak preserves inherent variability in the slip distribution, abrupt gradients in surface slip between fault sections (Figures 8 and 12) may indicate a relatively short surface rupture or a response to structural complexity. Abundant small offsets ( $< 3$  m) observed in the field typically coincide with rupture terminations or an increase in fault complexity (e.g., fault relays, step-overs, grabens, and changes in fault strike) (supporting information Data Sets S1 and S2). For example, the relatively simple Independence trace produces the largest preserved lateral 1872 offsets, yet surface slip appears to decrease to the south on the subparallel Lone Pine fault and Diaz Lake sections, bounding the Owens Valley graben (Figures 11 and 12a). While frequent small to moderately-sized offsets tend to generate a complex first peak in COPD plots (Figure 10), summing measurements across rupture complexity yields higher displacement values for the 1872 earthquake, largely in support of previous studies. This pattern contrasts with surface slip compilations for more continuous surface ruptures along higher slip-rate faults, which produce relatively simple COPDs with broader peaks for cumulative offsets [e.g., Zielke et al., 2010; Klinger et al., 2011].

Third, an important caveat to our study stems from the resolution of available lidar data for Owens Valley, which places a limit on our ability to resolve small earthquake surface displacements preserved in the landscape. Given an average return density of 4.6 returns/m<sup>2</sup>, we consider  $\sim 1$ –1.5 m as the minimum resolvable lateral offset for the area. Although 1872 slip was typically 2–3 times this value on average, small ( $< 1.5$  m) lateral offsets identified in areas of distributed faulting may be indistinguishable in the lidar compared to deflections of similar magnitude (e.g., the Tinemaha section, supporting information Figure S9). When observed in combination, two small offsets can resemble a single, larger displacement (e.g., Site HA08755 in supporting information Data Set S2). Our field investigations call attention to this resolution issue, which produces broader uncertainties for small offsets ( $< 6$  m) in particular.

An additional source of potential ambiguity in the lidar results from the oblique nature of OVF slip, thus promoting different rates of erosion or deposition on footwall and hanging wall surfaces. Post-earthquake

incision and scarp retreat potentially mute or conceal smaller geomorphic offsets through deposition on the downthrown hanging wall [e.g., *Lubetkin and Clark*, 1988]. Ongoing erosion and deposition over the course of more than one earthquake can lead to subtle asymmetrical alluvial fans and complex channel geometries on the hanging wall, particularly along the Lone Pine and Fish Springs faults. Although footwall surfaces may accumulate a relatively thick eolian cap, fault scarps along the valley floor promote ponding, incision and aggradation on downthrown surfaces [*Beanland and Clark*, 1994; *Bacon and Pezzopane*, 2007]. Because numerous scarps at elevations below  $\sim 1131$  m presumably formed under water during the PE [*Bacon et al.*, 2014], present-day scarp morphologies may conceal vertical separations related to prehistoric earthquakes (Figure 10) [*Bacon and Pezzopane*, 2007]. In an effort to capture the inherited slope as accurately as possible, we generally position fault-parallel profile lines further from the scarp on the hanging wall than on the footwall surface. Although we note no strong correlations between lateral offset magnitude and confidence (supporting information Figure S14), the ongoing evolution of geomorphic surfaces may account for significant variability in measured throw across offset features (Figure 10).

## 5.2. Comparison With Previous Studies

Overall, our calculated 1872 slip distribution (Figures 11 and 12) compares favorably with and fills broad data gaps in previous field-based studies [*Lubetkin and Clark*, 1988; *Beanland and Clark*, 1994]. Because our binned COPDs rely on a greater number of geomorphic markers, we reinterpret several previously published offsets associated with the 1872 earthquake as likely reflecting cumulative displacement in multiple events. Notably, the  $\sim 14$  m lateral offset of Diaz Creek (Figure 1, Site HA03229a in supporting information Data Set S2) reported by *Beanland and Clark* [1994] is consistent with large offsets adjacent to Diaz Creek, reflecting cumulative slip, perhaps over the past three earthquakes (supporting information Figure S5). Based on the lidar data, we recognize smaller lateral offset of the modern channel thalweg at this site ( $3.9 +0.5/-1$  m) (Site HA03230c in supporting information Data Set S2) similar in magnitude to nearby offsets populating the first strong peak in the COPD (supporting information Figure S5). Similarly, the 6–8 m lateral offset affecting the thalweg of the well-studied Lone Pine Creek (LPC3, Figure 2, Site HA03704l in supporting information Data Set S2) likely reflects cumulative slip in two events given the magnitude of offset peaks in the COPD attributed to 1872 and prehistoric earthquakes (Figure 11c and supporting information Figure S5). 1872 offsets at confident sites to the north and south vary up to  $\sim 5$  m (e.g., Sites HA02983a, HA02999b, HA02999c, HA03230c, HA03443a, HA03938d, and HA04151f) and contribute to a relatively broad first peak with a shoulder encompassing offsets with errors up to  $\sim 6$  m. Recalculation of boulder ages from *Bierman et al.* [1995] and *Bacon and Pezzopane* [2007] demonstrates activity of the faulted Lone Pine fan between  $\sim 10$  and 24 ka. LPC3 incised the oldest surfaces prior to the development of LPC2 (Figure 2b) [*Bierman et al.*, 1995] and appears to record a total of three faulting events [e.g., *Lubetkin and Clark*, 1988].

Along the Independence section of the OVF, we revisited another relatively large ( $7.5 \pm 1.1$  m) channel offset at an elevation of 1152 m, first assigned to 1872 by *Beanland and Clark* [1994] (Site HA06319n in supporting information Data Set S2). Given the range of uncertainty predicted by the broad channel, we find that the well-known offset contributes to an equivocal second peak in the binned COPD (Figure 9d and supporting information Figure S8). Because the paleoseismic record for the central OVF [*Lee et al.*, 2001a] indicates two late Holocene surface-rupturing earthquakes, we tentatively classify this and similar  $>6$  m geomorphic offsets along the central OVF as cumulative displacements, incorporating  $\sim 5$ –6 m of 1872 slip and a possible PE with relatively low slip ( $\sim 2$  m). Although the adjacent scarp is relatively high ( $\sim 4$  m), the apparent separation may incorporate some undercutting of the Owens River (Site HA06319n in supporting information Data Set S2) [e.g., *Bacon and Pezzopane*, 2007].

Our expanded record documented at previously unrecognized sites along the Lone Pine fault reveals that the location and average value of net displacement is similar to past interpretations. We derive the net amount of 1872 surface slip by summing distributions for the OVF and LPF compiled along average fault strike (Figure 13). This estimate assumes an  $80^\circ$  dipping fault plane and omits contributions due to warping or vertical axis block rotations between the Diaz Lake and LPF. We average slip measurements within 5-km bins, filling in graphically for gaps between higher confidence data [e.g., *Haessler et al.*, 2004], and estimate an average total displacement of  $4.4 \pm 1.5$  m ( $2\sigma$ ) (supporting information Table S4). We find an increase in net 1872 displacement south of Independence approaching a maximum in net slip of approximately  $9 \pm 2$  m, achieved just north of Lone Pine (Figure 13c). This  $\sim 7$ –11 m range agrees well with the estimate

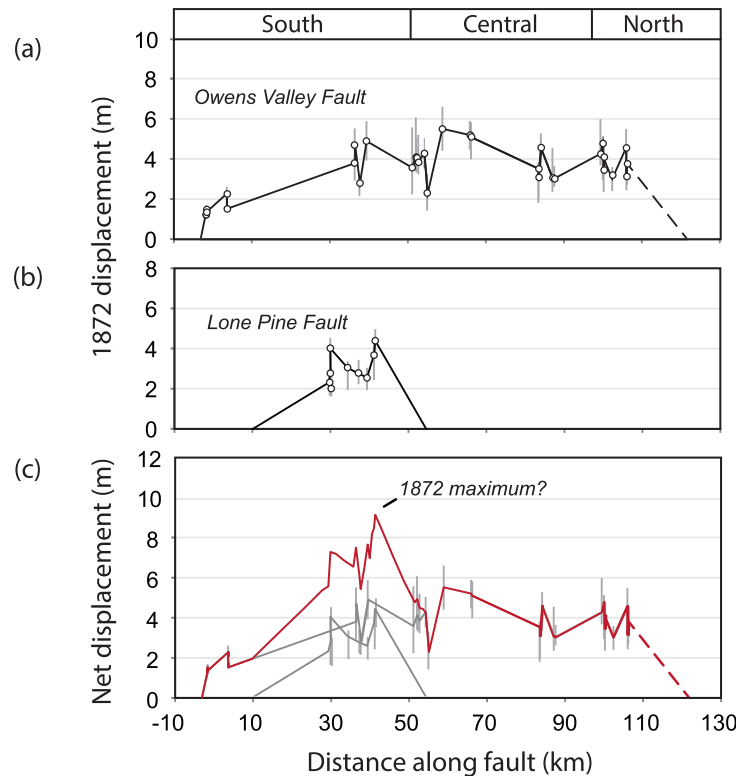


**Figure 13.** Net 1872 surface slip derived from moderate to high confidence displacements plotted along subparallel strands. Gray bars reflect aggregated uncertainties from back-slipping of lidar imagery. (a) Along-strike compilation of displacement values for main traces of the OVF, as predicted by binned COPD plots. (b) Along-strike compilation of Lone Pine fault displacements. (c) Summed distributions (red lines) for possible net 1872 surface slip along a simplified fault plane striking 340° and dipping 80° northeast. The maximum implied displacement is between 7 and 11 m and reflects the average of four high values. The net slip averages  $4.4 \pm 1.5$  m based on a 5-km binned average that incorporates graphical values for gaps between higher confidence data.

reported by *Lubetkin and Clark [1988]* and is similar to recent findings for the Landers and Hector Mine earthquakes [*Sieh et al., 1993; Treiman et al., 2002*].

Our data set enables us to provide the first reconstructions of surface slip associated with prehistoric Owens Valley earthquakes (Figure 11). Although patterns of single-event and cumulative displacement along the northern and southern sections of the fault are similar, the extent of these ruptures is less clear due to gaps in the surface paleoseismic record along the central OVF (Figure 11). Lateral offsets compiled along central traces contribute to two closely spaced clusters between ~4 and 8 m (Figure 10d and supporting information Figures S7 and S8). Here we consider three possible explanations for this distribution. First, the offsets could

stem from short-wavelength variability along the 1872 rupture alone near the Owens River, leading to a bimodal peak in the lateral COPD (Figures 11 and 13 and supporting information Figures S7 and S8). Less than ~1 m of measured throw along the southern Independence section suggests only one rupture along this trace, consistent with trenching by *Beanland and Clark [1994]* (supporting information Figure S7). Second, the slip cluster could reflect ~5 m of slip during 1872 and a smaller amount related to a previous surface rupture coeval with the ~9 ka PE resolved near Lone Pine [*Bacon and Pezzopane, 2007*]. Throw measurements across the Independence section varying from ~0.5 to 1.8 m support this interpretation (supporting information Figure S8). A third possible explanation is that the subsidiary peak represents relatively low-magnitude PE slip near Independence with slip tapering to the south, consistent with evidence for two late Holocene earthquakes resolved in trench exposures near Independence [*Lee et al., 2001a*] (Figures 1 and 11). Similarity in the possible timing of the central OVF PE [*Lee et al., 2001a*] and the White Mountain fault MRE estimated at ~3 ka [*dePolo, 1989*] may favor this interpretation, suggesting that distributed WMF slip may influence the OVF slip distribution in this area [*Bacon and Pezzopane, 2007*].

Surface slip distributions along the northernmost OVF do not exhibit a taper or recurring gradient near Klondike Lake approaching the ~2–5 km wide releasing stepover to the White Mountain fault (Figure 11). Although our data do not preclude a steep gradient with a possible rupture termination at the northeast-striking Klondike Springs fault (Figure 11), apparently high recurrent slip may indicate continued partial or full rupture toward Bishop Creek [e.g., *Elliott et al., 2009*]. Distributions for the northern OVF may also include surface slip related to moderate or large earthquakes on nearby normal and normal-oblique faults (e.g., WMF, SNFF, and FSF) (Figure 1). Relatively fresh scarps along the southern WMF attributed to 1872 [*Carver, 1970*] suggest the potential for overlapping surface rupture across OVF–WMF system. The

chronology of past earthquakes along the northern OVF, Keough section, and the southern Fish Slough fault is unknown and currently offers little context for Holocene scarps extending into Bishop (Figures 1 and 8) [e.g., Bryant, 1984b]. As such, the northward extent of 1872 and prehistoric OVF ruptures remains relatively unconstrained [Slemmons et al., 2008].

### 5.3. Comparison Between 1872 and Earlier Ruptures

Despite questions surrounding the overall extent of past OVF surface ruptures, our findings suggest some consistency amongst point displacements for large Owens Valley ruptures. Notably, the average peak spacing between lateral and vertical offset clusters in the net and binned COPD plots spanning the LPF and northern OVF is  $\sim 4$  and  $\sim 0.9$  m, respectively, for the last three peaks (Figures 10 and 11). Although the chronology of prehistoric events in northern Owens Valley is unknown, the existing paleoseismic record for the southern OVF favors displacements similar in magnitude and style for the past three earthquakes [Lubetkin and Clark, 1988; Bacon and Pezzopane, 2007]. The gradual decrease or dogtail taper [Ward, 1997] in 1872 surface slip south of Lone Pine is consistent with rupture termination north of the  $\sim 7$  km wide discontinuity in Rose Valley (Figures 1, 11, and 13) [e.g., Elliott et al., 2009]. The timing of the most recent event on the Sage Flat fault between 25.7 and 30.1 ka [Amos et al., 2013a] may indicate a similar terminus for the PE on the southern Owens Valley fault, as well. (Figure 1).

Uncertainty in the overall shape of slip distributions for the central OVF, however, leaves open the possibility that past surface ruptures spanned variable lengths. In general, the ephemeral nature of small geomorphic offsets [e.g., Zielke et al., 2015] suggests a potential inability to resolve partial or moderate earthquake ruptures in the geomorphic record. Closely spaced peaks apparent in the binned COPD plots for the central OVF, however, could reflect a southward taper in relatively low-magnitude cumulative PE slip above the detection limit for this study (Figure 11). Given the ambiguity associated with the higher-offset lateral peak between 6–8 m (Figure 10 and supporting information Figures S7 and S8), evidence consistent with large penultimate earthquakes that contrast in timing and extent for the southern and central Owens Valley [Lee et al., 2001a; Bacon and Pezzopane, 2007] suggests the need for further testing in the subsurface.

Our reconstructions of surface slip based on offset peaks highlight important questions about the geomorphic record of slip variability associated with multiple earthquakes and the impact on long-term patterns of strain release. Notably, the breadth of the cumulative PE peak in the lateral COPDs (Figures 10 and 11) appears muted in comparison to the relatively broad first peak, which comprises a greater number of relatively fresh offsets. One explanation for the considerably narrower second peak is selective preservation of cumulative offsets, whereby ongoing surface processes favor relatively discrete, higher-confidence offsets. Thus, the existing geomorphic record may not represent the overall amount and style of cumulative slip, particularly along complex surface traces in relatively active geomorphic environments. Another explanation for the narrower second peak introduces the possibility of overlapping values corresponding to single- and multiple-event displacements. Such variability leads to ambiguities in straightforward interpretations of net COPD plots and may provide insight into the multimodal nature of the cumulative APE peak, possibly reflecting compounded effects of heterogeneous and distributed surface slip over an increasing number of earthquakes (Figure 10). Despite the likelihood of selective preservation and overlap among event displacements, the positive correlation overall between throw and lateral offset supports the interpretation that our data reflect both single-event and cumulative displacements (Figure 9).

Similar short-wavelength variability in measured throw values apparently produces considerable overlap among offset clusters (Figures 8c, 10 and supporting information Figure S13b) and complicates the overall picture of cumulative vertical deformation associated prehistoric earthquakes. This variability may reflect a variety of potential long-term sources aside from post-earthquake modification of the scarp. First, the dominant lateral component of slip may juxtapose topography and produce errant measurements in the measured vertical component. Because LaDiCaoz\_v2 involves tracing of sublinear features on either side of the fault and accounts for the lateral shift of these features, we can confidently rule out this juxtaposition of topography in our data set. For example, our data along the Lone Pine fault improve the overall surface slip pattern depicted by 1872 and cumulative vertical separations from scarp profiles (supporting information Figure S5e) [Lubetkin and Clark, 1988]. Second, some of the vertical component along the OVF may arise from lateral spreading or other shallow ground disturbance unrelated to fault slip. Such deformation is widespread along portions of the southern OVF, especially flanking the former margins of Owens Lake

[e.g., Carver, 1970; Bacon *et al.*, 2003]. As such, we exclude from our analysis well-defined arcuate geomorphic scarps west of Owens Lake and along the Manzanar fault (supporting information Data Set S1). Third, geometric complexity in the highly segmented rupture trace may lead to variability in the recorded vertical deformation unrelated to the overall oblique nature of fault displacement. We note the presence of a smaller number of west-facing scarps (Figure 8) that correspond directly to surface complexity between en echelon traces of the Owens Valley fault. Numerous stepovers, fault splays, and linear grabens visible in our fault mapping distribute and partition slip (supporting information Data Set S1), indicating that local fault complexity contributes to measured variability for both east and west facing scarps.

Lastly, however, the predominance of east-facing scarps (Figure 8c) suggests the prevailing influence of overall fault geometry in controlling vertical offset along the OVF. Both the steep, northeastward dip of the fault and its clockwise orientation with respect to the northwestward pattern of regional shear (Figure 1) [Lifton *et al.*, 2013] contribute to a slight overall releasing geometry for the OVF [Wesnousky and Jones, 1994; Unruh *et al.*, 2003]. This fault orientation results in relatively high average lateral to vertical ratios during 1872 (Figure 11c) with significant variability both compounding and masking the overall pattern of vertical deformation in previous events. As such, we consider clusters in the vertical COPD plots (Figure 9) as being subordinate to the lateral offsets for choosing common values corresponding to single and multiple-event displacements along similar, oblique-slip faults.

#### 5.4. Implications for Earthquake Magnitude

Understanding the geomorphic record of past Owens Valley ruptures bears directly on questions surrounding the magnitude and overall moment release during 1872. Seismic moment is the product of the shear modulus ( $3 \times 10^{11}$  dyn·cm<sup>-2</sup>), average slip at depth (~4.4 m), and fault rupture area. We derive the latter based on the range of recognized rupture lengths (113–120 km), the average ~80° dip [Beanland and Clark, 1994], and the maximum depth range of earthquakes in the region. Given the general absence of seismicity along the 1872 rupture [Hough and Hutton, 2008], we estimate a seismogenic depth of  $15 \pm 5$  km based on seismicity cross sections for the ECSZ through Landers, Barstow, and northern Owens Valley [Hauksson and Shearer, 2005; Phillips and Majkowski, 2011]. These preferred values yield a geologic seismic moment release of  $\sim 2.3 \times 10^{27}$  dyn·cm, with estimates between  $1.0 \times 10^{27}$  dyn·cm and  $4.3 \times 10^{27}$  dyn·cm. Using the formula of Hanks and Kanamori [1979] for moment magnitude, we calculate a preferred magnitude for the 1872 earthquake of  $M_w$  7.5, with a range encompassing values between  $M_w$  7.3 and 7.7. Despite lower average slip, this estimate overlaps with the  $M_w$  7.5–7.7 determined by Beanland and Clark [1994] and  $M_w$  7.4–7.5 by Bakun [2006].

The displacement-to-length (D:L) ratio calculated for 1872 based on our improved parameters—e.g., total average displacement ( $4.4 \pm 1.5$ ) and range of rupture lengths (~113–120 km)—is between  $2.4 \times 10^{-5}$  and  $5.2 \times 10^{-5}$  (likely  $3.9 \times 10^{-5}$ ). Our preferred value is within  $1\sigma$  of the global average ( $1.6 \times 10^{-5} \pm 4.4 \times 10^{-5}$ ) calculated using the data set of Wesnousky [2008] and Biasi *et al.* [2013], but in excess of D:L ratios for great San Andreas earthquakes by a factor of four. Comparison with other historical ruptures [Rodgers and Little, 2006; Wesnousky, 2008; Biasi *et al.*, 2013; Gold *et al.*, 2015] places 1872 Owens Valley surface slip at the higher end of the envelope defined by strike-slip ruptures in California and across the globe (Figure 14). 1872 slip-length parameters are generally more similar to ruptures occurring in slowly deforming continental interiors (e.g., WL, ECSZ, and New Zealand).

Explanations for a higher D:L ratio include a relatively high static stress drop [e.g., Quigley *et al.*, 2012] or rupture with a lower (i.e., more circular) L/W aspect ratio [e.g., Rodgers and Little, 2006]. Similar D:L ratios for the Landers ( $4.4 \times 10^{-5}$ ) and Hector Mine ( $4.5 \times 10^{-5}$ ) earthquakes may reflect the influence of fault strength on static stress changes. Geodetic inversions for the Landers and Hector Mine earthquakes point to relatively high static stress drops [Price and Bürgmann, 2002], possibly related to the relative structural immaturity of faults within the southern Walker Lane or ECSZ [e.g., Scholz *et al.*, 1986; Kanamori and Allen, 1986]. Large earthquakes in this relatively low strain rate region [e.g., Oskin *et al.*, 2007] exhibit millennial return times (~5–15 ka) [Rockwell *et al.*, 2000]. Historic surface ruptures typically span a number of geometric segments, including faults previously unmapped or considered inactive over the Holocene [Bell *et al.*, 1999; Caskey *et al.*, 1996; Sieh *et al.*, 1993; U.S. Geological Survey, the Southern California Earthquake Center, and the California Division of Mines and Geology, 2000; Treiman *et al.*, 2002; Quigley *et al.*, 2012]. The corresponding seismologically determined moment release during these events is generally larger than expected [e.g., Hough and Hutton, 2008] and may exceed empirical predictions based on geologic observations of D:L ratios [e.g., Quigley *et al.*, 2012]. Additional insight into the seismogenic depth and

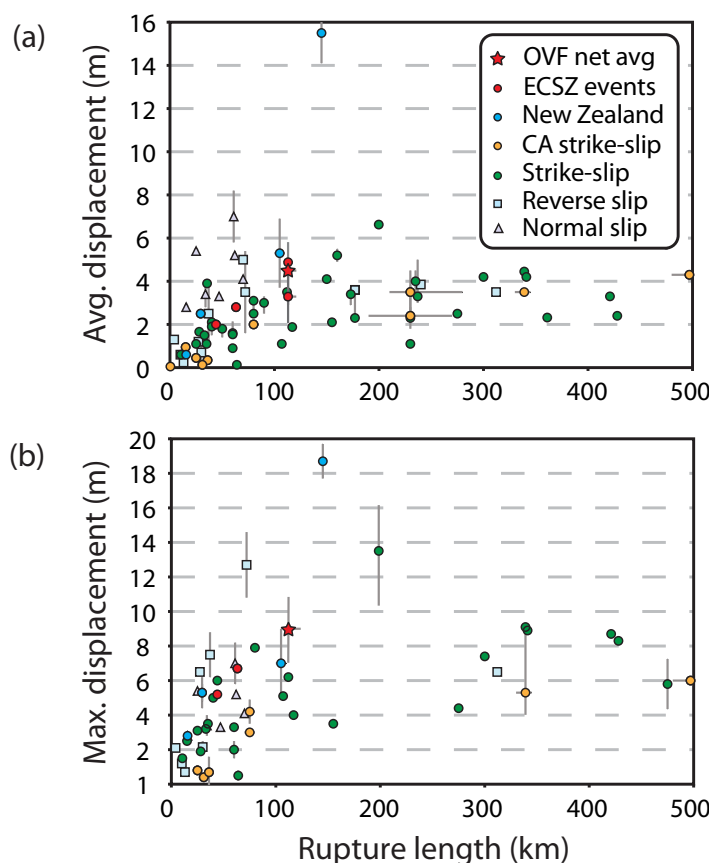


**Figure 14.** Comparison of 1872 slip-length parameters for well-studied earthquakes worldwide adapted from *Wesnousky* [2008] and *Biasi et al.* [2013]. Plots show (a) average net displacement values and (b) maximum net displacements, including the 1872 Owens Valley earthquake (red stars). The 1872 rupture length ranges from 113–120 km [*Slemmons et al.*, 2008]. Symbols indicate continental reverse-slip (blue squares), normal-slip (purple triangles), and strike-slip events (green points). Plotted separately are predominantly strike-slip ruptures in California (yellow points), New Zealand (turquoise points), and the eastern California shear zone (ECSZ) (red points), including the 1872 estimate by *McCalpin and Slemmons* [1998] (MS98) and our average value for distributed slip ( $3.3 \pm 1.1$  m). Gray bars indicate reported uncertainties.

overall subsurface configuration of faults that actively partition slip [e.g., *Wesnousky and Jones*, 1994; *Caskey et al.*, 1996; *Henry et al.*, 2007] may shed light on the potential for wider rupture and the energetic nature of ground motions felt during the 1872 earthquake.

### 5.5. Implications for Owens Valley Fault Slip Rates

Our database of geomorphic offsets also enables estimates of time-averaged slip for the Owens Valley from the late Quaternary to latest Holocene. Although our study does not provide new dates for offset landforms, we capitalize on the wealth of previously dated features forming the Owens Valley geomorphic surface [*Turrin and Gillespie*, 1986; *Bierman et al.*, 1995; *Bacon et al.*, 2003, 2006, 2013, 2014; *Benn et al.*, 2006; *Dühnforth et al.*, 2007; *Le et al.*, 2007; *Jayko and Bacon*, 2008; *Kirby et al.*, 2008; *Orme and Orme*, 2008]. These ages come from dated shorelines, alluvial fans, debris-flow boulders, etc., providing a clear geomorphic and stratigraphic context for evaluation of our measured offsets (supporting information Table S5).

The simplest proxy for landform age in Owens Valley is elevation within the basin. Oscillations in the level of pluvial Owens Lake since the late Pleistocene record an overall decrease in lake level elevations and reworking of the basin surface. Surface processes subsequently superimpose and inset younger geomorphic features on abandoned lacustrine surfaces, resulting in a landscape with composite ages. Although pluvial highstands do not likely remove all evidence of older landforms, overall declining lake levels suggest that displaced landforms at higher elevations within the basin surface are likely older and record cumulative displacements. Smaller displacements on these older surfaces can then be explained by subsequent landform incision or deposition on an older surface.

Oblique OVF displacements plotted as a function of surface age generally distribute beneath a maximum envelope defined by a linear fit to the largest offsets (Figure 15). We view the largest offsets for each surface as nearest in age to the corresponding geochronologic date or pluvial highstand indicated by the elevation of dated Pleistocene shorelines (supporting information Table S5). Apparent large lateral offsets occupying younger surfaces (e.g., Sites HA2891b and HA03279a in supporting information Data Set S2) [*Beanland and Clark*, 1994] may be landforms submerged during an earlier highstand of the Owens Lake and reworked or eroded by water, potentially contributing to relatively low scarps (e.g., Sites HA7700b, HA7834a, HA7847b, and HA07964c in supporting information Data Set S2). We extend the stated uncertainties for these apparent large offsets to incorporate the age bracket suggested by similar offsets (Figure 15a). Taken together, we see

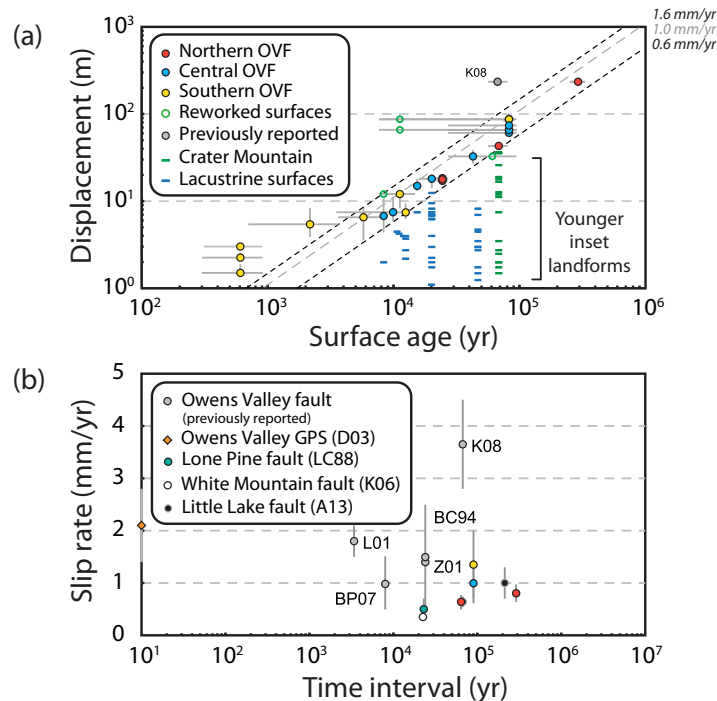


**Figure 15.** Owens Valley fault slip rates estimated from cumulative surface slip measurements combined with previously published ages for geologic features and geomorphic surfaces in Owens Valley. Ages, elevations, and references for these dates are provided in supporting information Table S5. (a) Linear regressions indicate the suggested range of average lateral-oblique slip rates between  $\sim 0.6$  and  $1.6$  mm/yr for the northern (red,  $\sim 0.7$  mm/yr), central (blue,  $\sim 1.0$  mm/yr), and southern (yellow,  $\sim 1.3$  mm/yr) fault sections. Displacements reflect optimum values and associated uncertainties derived from the lateral and vertical offset and average fault dip ( $80^\circ$ ). Points also represent optimum ages or preferred values for surfaces formed over a single MIS interval. Horizontal gray bars reflect the breadth of the MIS interval or range of reported uncertainties. For large offsets occupying apparently young surfaces (hollow points), uncertainties also incorporate the likely surface age prior to the last pluvial highstand. Smaller offsets (dashes) represent features formed on lacustrine surfaces (blue) or Crater Mountain basalts (green). (b) Compilation of fault slip rates for the southwestern Walker Lane plotted against age, including the OVF, Lone Pine fault (LPF), and adjoining normal-oblique White Mountain fault and dextral Little Lake fault. We derive an additional rate for the northern OVF ( $\sim 0.8$  mm/yr) based on dextral offset from Kirby *et al.* [2008] ( $235 \pm 15$  m) and age from Turrin and Gillespie [1986] ( $290 \pm 40$  ka). A13, Amos *et al.* [2013b]; BC94, Beanland and Clark [1994]; BP07, Bacon and Pezzopane [2007]; D03, Dixon *et al.* [2003]; K06, Kirby *et al.* [2006]; K08, Kirby *et al.* [2008]; L01, Lee *et al.* [2001a]; LC88, Lubetkin and Clark [1988]; Z01, Zehfuss *et al.* [2001].

*et al.*, 1995]. As such, future work on long-term slip history will continue to bear on predictive models for Owens Valley earthquake recurrence.

Fault slip between  $\sim 0.6$  and  $1.6$  mm/yr since the late Quaternary is consistent with the rate and style of regional deformation for adjoining structures delineating the eastern margin of the Sierra Nevada microplate (Figure 16). To the south, average lateral slip on the Little Lake fault (Figure 1) occurs at a rate of  $\sim 0.6$ – $1.3$  mm/yr since the mid-to-late Pleistocene [Amos *et al.*, 2013b]. Integrating rates across southern Owens Valley section may increase the slip rate near Lone Pine by up to  $0.5 \pm 0.2$  mm/yr [Lubetkin and Clark, 1988]. The Deep Springs fault accommodates slip transferred north of the OVF and across the White Mountains to the Fish Lake Valley Fault (Figure 16) [Reheis and Dixon, 1996]. Summed rates of late Pleistocene oblique slip on the WMF of  $0.3$ – $0.4$  mm/yr [Kirby *et al.*, 2006] and normal slip on the Deeps Springs fault ( $\sim 0.7$  mm/yr) [Lee *et al.*, 2001b] are also consistent with our suggested time-averaged OVF slip rate. This snapshot of late Quaternary slip rates suggests a slight northward taper as fault slip transfers from the OVF onto other prominent structures in the southwestern Walker Lane (Figure 16). We speculate that the maintenance of this taper in strain release involves relatively large OVF ruptures perhaps similar to 1872 or the inclusion of additional moderate earthquakes without a strong geomorphic signal preserved in the landscape.

strong evidence for decreased offset of progressively younger, inset surfaces. The maximum offsets and corresponding age brackets suggest an average lateral-oblique slip rate between  $0.6$  and  $1.6$  mm/yr ( $1\sigma$ ) over the late Quaternary to latest Holocene (Figure 15a). Only the youngest Holocene ( $<3$  ka) landforms presumably affected by only the 1872 event fall above the trend line, given the incomplete earthquake cycle since the most recent event.

Time-averaged slip rates between  $\sim 0.6$  and  $1.6$  mm/yr overlap with previous estimates from late Quaternary and Holocene geologic features [Lubetkin and Clark, 1988; Beanland and Clark, 1994; Lee *et al.*, 2001a; Bacon and Pezzopane, 2007] and suggest relatively steady slip over this period (Figure 15b). If large slip rate variations implied by other studies [e.g., Kirby *et al.*, 2008] do not occur,  $\sim 4$  m of average slip per event accumulating at a rate of  $\sim 1$  m per kyr suggests more frequent earthquakes than recently documented on the southern OVF, corresponding to an average return time of  $\sim 4$  ka [Beanland and Clark, 1994; Lee *et al.*, 2001a; Bierman

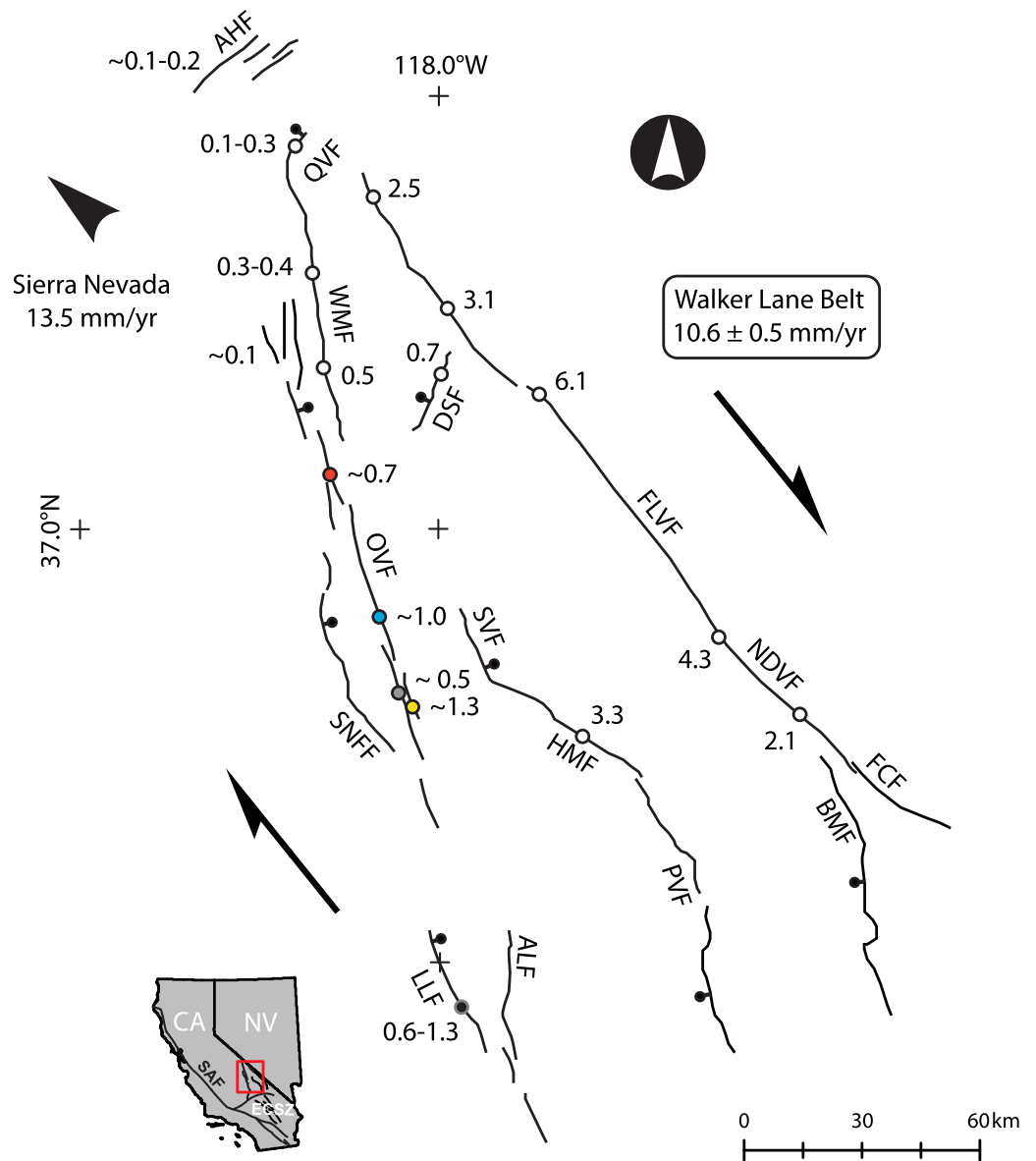


**Figure 16.** Compilation of reported slip rates in mm/yr on active faults in the southern Walker Lane (modified from Foy *et al.* [2012]) with respect to the geodetic rate across the zone derived from the global positioning system and the relative motion of the Sierra Nevada–Great Valley microplate [Lifton *et al.*, 2013]. Geologic slip rate studies, from south to north: Amos *et al.* [2013b], (this study), Oswald and Wesnousky [2002], Frankel *et al.* [2007a,b], Lubetkin and Clark [1988], Reheis and Sawyer [1997], Lee *et al.* [2001b], Ganey *et al.* [2010], Kirby *et al.* [2006], and Nagorsen-Rinke *et al.* [2013]. Faults listed alphabetically: AHF, Adobe Hills fault; ALF, Airport Lake fault; BMF, Black Mountain fault; DSF, Deep Springs fault; FCF, Furnace Creek fault; FLVF, Fish Lake Valley fault; HMF, Hunter Mountain fault; LLF, Little Lake fault; OVF, Owens Valley fault; NDVF, Northern Death Valley fault; PVF, Panamint Valley fault; QVF, Queen Valley fault; SAF, San Andreas fault; SNFF, Sierra Nevada frontal fault; SVF, Saline Valley fault; WMF, White Mountain fault.

## 6. Conclusions

Geomorphic characterization and compilation of offset landforms from lidar and field data provide a record of at least three Owens Valley surface ruptures in a timespan of 25 kyr. Landform development and modification in the Owens Valley is largely controlled by climatic oscillations and bears a strong imprint of corresponding fluctuations and reworking by pluvial Owens Lake. As such, the relatively diverse geomorphic surface of the Owens Valley may provide a relatively continuous and perhaps less ambiguous surface paleoseismic record compared to higher slip rate faults with centennial recurrence intervals. As such, we suggest that landforms in the Owens Valley likely capture at least the largest surface-rupturing earthquakes and that cumulative offsets along the OVF are most simply interpreted as reflecting large events.

Our new lidar analysis tool, LaDiCaoz\_v2, quantifies offset measurements and associated errors and produces cumulative offset probability distribution (COPD) plots that complement the existing paleoseismic record for earthquake recurrence in Owens Valley. Measurements compiled along the most recent 1872 Owens Valley rupture imply an average dextral surface offset of  $3.3 \pm 1.1$  m and predominantly east-down vertical throw of  $0.8 \pm 0.5$  m. Summing these average displacements across subparallel strands, however, demonstrates higher net surface displacements of  $4.4 \pm 1.5$  m. Maximum surface displacements north of Lone Pine ( $\sim 7$ – $11$  m) overlap with recent findings for historical ECSZ events. Consideration of rupture parameters for previous historical San Andreas earthquake ruptures suggests a relatively high 1872 displacement-to-length (D:L) ratio. Given the steep, northeastward dip of the fault, our findings are consistent overall with a relatively high stress drop earthquake occurring in a structurally immature and evolving deformation zone within the southern Walker Lane.

Our new results for coseismic displacement ( $\sim 4.4$  m) and rupture length ( $\sim 113$ – $120$  km) for the 1872 earthquake yield a refined geologic moment magnitude estimate with a preferred  $M_w$  7.5 and a plausible range between  $M_w$  7.3 and 7.7. Despite modification of geomorphic surfaces and fault scarps along the valley floor, we demonstrate that cumulative dextral offsets at higher elevations remain preserved in the geomorphic record. Higher-offset lateral peaks including previous large earthquakes suggest average cumulative offsets of  $7.1 \pm 2.0$  m,  $12.8 \pm 1.5$  m, and  $16.6 \pm 1.4$  m. Although well-preserved average displacements for northern and southern Owens Valley earthquakes imply continuous past ruptures, the shape of our distributions leaves open the possibility of earthquakes with distributed slip and more along-strike variability.

Given changes in fault orientation and the presence of multiple en echelon and overlapping surface ruptures, reconstructions of along-strike gradients in displacement require analysis of binned COPDs for individual sections of the fault. We also emphasize the importance of field verification for testing hypotheses related to slip variability along strike. Complex OVF geometries contribute to multimodal COPDs, which may cause ambiguity for smaller offsets approaching the resolution limit of typical lidar-based studies ( $\sim 1$ – $1.5$  m). For sites where multiple strands offset a single geomorphic feature, COPDs should incorporate summed measurements. Variability in the vertical component of surface slip highlights both localized rupture complexities and the ongoing effects of erosion and deposition along the fault scarp. Ultimately, the prevailing influence of fault orientation with respect to the regional pattern of dextral shear results in predominately east-facing scarps along the OVF. Compound variability in the vertical data limits the utility of vertical offsets for discerning prehistoric earthquakes along oblique-slip faults and determining slip ratios during these events.

Viewed in context with previously published ages, our offset database suggests average rates of fault slip from  $\sim 0.6$  to  $1.6$  mm/yr ( $1\sigma$ ) over the late Quaternary. Although apparently relatively steady over time, these slip rates define an overall northward decrease as the OVF terminates and distributes slip onto other structures. This taper in strain release may be sustained by recurring large earthquakes and additional moderate events unresolved by this study. Viewed in context with other active structures in the region, our results depict an overall pattern of spatially variable strain release along individual faults, thus providing a potentially coherent snapshot of regional rates of dextral and normal-oblique faulting for nearby and adjoining structures along the eastern margin of the Sierra Nevada–Great Valley microplate.

## References

- Akçiz, S. O., L. G. Ludwig, J. R. Arrowsmith, and O. Zielke (2010), Century-long average time intervals between earthquake ruptures of the San Andreas fault in the Carrizo Plain, California, *Geology*, *38*(9), 787–790, doi:10.1130/g30995.1.
- Amos, C. B., D. W. Burbank, and S. A. Read (2010), Along-strike growth of the Ostler fault, New Zealand: Consequences for drainage deflection above active thrusts, *Tectonics*, *29*, TC4021, doi:10.1029/2009TC002613.
- Amos, C. B., A. T. Lutz, A. S. Jayko, S. A. Mahan, G. B. Fisher, and J. R. Unruh (2013a), Refining the southern extent of the 1872 Owens Valley Earthquake Rupture through paleoseismic investigations in the Haiwee area, Southeastern California, *Bull. Seismol. Soc. Am.*, *103*(2A), 1022–1037, doi:10.1785/0120120024.
- Amos, C. B., S. J. Brownlee, D. H. Rood, G. B. Fisher, R. Bürgmann, P. R. Renne, and A. S. Jayko (2013b), Chronology of tectonic, geomorphic, and volcanic interactions and the tempo of fault slip near Little Lake, California, *Geol. Soc. Am. Bull.*, *125*(7–8), 1187–1202, doi:10.1130/B30803.1.
- Bacon, S. N., and S. K. Pezzopane (2007), A 25,000-year record of earthquakes on the Owens Valley fault near Lone Pine, California: Implications for recurrence intervals, slip rates, and segmentation models, *Geol. Soc. Am. Bull.*, *119*(7–8), 823–847, doi:10.1130/B25879.1.
- Bacon, S. N., S. K. Pezzopane, and R. M. Burke (2003), Paleoseismology on the Owens Valley fault and latest Quaternary stratigraphy in Owens Valley near Lone Pine, eastern California, US Geological Survey, National Earthquake Hazards Reduction Program (NEHRP) Final Technical Report, 42 pp. [Available at <http://erp-web.er.usgs.gov/reports/abstract/2002/ni/02hqgr0003.pdf>.]
- Bacon, S. N., R. M. Burke, S. K. Pezzopane, and A. S. Jayko (2006), Last glacial maximum and Holocene lake levels of Owens Lake, eastern California, USA, *Quat. Sci. Rev.*, *25*(11–12), 1264–1282, doi:10.1016/j.quascirev.2005.10.014.
- Bacon, S. N., N. Lancaster, S. Stine, E. J. Rhodes, and G. A. M. Holder (2013), Refined late Holocene lake-level history of Owens Lake, east-central California, *Geol. Soc. Am. Abstr. Programs*, *45*(7), 552.

## Acknowledgments

Data sets and expanded results contributing to this study are available in the supporting information. The EarthScope Southern and Eastern California Lidar Project (available online at <http://opentopo.sdsc.edu>) involved data acquisition and processing for the Plate Boundary Observatory (PBO) by NCALM (<http://www.ncalm.org>). UNAVCO operates the PBO for EarthScope (<http://www.earthscope.org>), supported by the National Science Foundation (EAR-0350028 and EAR-0732947). Funding for this study was provided by the Southern California Earthquake Center (SCEC) (Project 12140), the Geological Society of America Graduate Student Research fund, the Community Foundation of San Bernardino county, and the Western Washington University Geology Department. We thank G. Seitz, M. Price, and K. Morgan for assistance in the field, and S. Bacon, J. Arrowsmith, R. Weldon, K. Scharer, J. Unruh, C. Madden-Madugo, and D. Haddad for helpful discussions. Constructive reviews by D. Schwartz, R. Briggs, E. Schermer, D. Clark, and one anonymous reviewer substantially improved the paper. We also thank the staff at the UC White Mountain Research Center for facilitating this work. Any use of trade, firm, or product names is for descriptive purposes only and does not imply endorsement by the U.S. Government.

- Bacon, S. N., K. D. Adams, T. F. Bullard, A. Keen-Zebert, and D. L. Decker (2014), Sill failure and catastrophic outburst floods from Owens Lake, California: Implications for latest Pleistocene and Holocene paleohydrology of the Owens River basin, *Geol. Soc. Am. Abstr. Programs*, 46(6), 746.
- Bakun, W. H. (2006), MMI attenuation and historical earthquakes in the basin and range province of western North America, *Seismol. Soc. Am. Bull.*, 96, 2206–2220, doi:10.1785/0120060045.
- Bateman, P. C. (1961), Willard D. Johnson and the strike-slip component of fault movement in the Owens Valley, California, *Seismol. Soc. Am. Bull.*, 51, 483–493.
- Beanland, S., and M. M. Clark (1994), The Owens Valley fault zone, eastern California, and surface rupture associated with the 1872 earthquake, *U.S. Geol. Surv. Bull.*, 1982, 29 pp.
- Bell, J. W., A. R. Ramelli, A. M. Sarna-Wojcicki, and C. E. Meyer (1999), Surface faulting and paleoseismic history of the 1932 Cedar Mountain earthquake area, west-central Nevada, and implications for modern tectonics of the Walker Lane, *Geol. Soc. Am. Bull.*, 111(6), 791–807.
- Bell, J. W., F. Amelung, and C. D. Henry (2012), InSAR analysis of the 2008 Reno-Mogul earthquake swarm: Evidence for westward migration of Walker Lane style dextral faulting, *Geophys. Res. Lett.*, 39, L18306, doi:10.1029/2012GL052795.
- Benn, D. I., L. A. Owen, R. C. Finkel, and S. Clemmens (2006), Pleistocene lake outburst floods and fan formation along the eastern Sierra Nevada, California: Implications for the interpretation of intermontane lacustrine records, *Quat. Sci. Rev.*, 25(21–22), 2729–2748, doi:10.1016/j.quascirev.2006.02.018.
- Biasi, G. P., R. J. Weldon, and T. E. Dawson (2013), Appendix F—Distribution of slip in ruptures, *U.S. Geol. Surv. Open File Rep.*, 1165, 65 pp.
- Bierman, P. R., A. R. Gillespie, and M. W. Caffee (1995), Cosmogenic ages for earthquake recurrence intervals and debris flow fan deposition, Owens-Valley, California, *Science*, 270(5235), 447–450, doi:10.1126/science.270.5235.447.
- Brossy, C. C., et al. (2012), Map of the late Quaternary active Kern Canyon and Breckenridge faults, southern Sierra Nevada, California, *Geosphere*, 8, 581–591, doi:10.1130/GES00663.1.
- Bryant, W. A. (1984a), Northern Owens Valley, Fish Slough, and White Mountains frontal faults, Inyo and Mono counties, California, in *California Division of Mines and Geology Fault Evaluation Reports, FER-153*, scale 1:24,000, 19 pp., Calif. Geol. Surv. [Available at <http://www.quake.ca.gov/gmaps/WH/regulatorymaps.htm>.]
- Bryant, W. A. (1984b), Owens Valley and White Mountains frontal fault zones, Big Pine area, Inyo County, California, in *California Division of Mines and Geology Fault Evaluation Reports, FER-159*, scale 1:24,000, 19 pp., Calif. Geol. Surv. [Available at <http://www.quake.ca.gov/gmaps/WH/regulatorymaps.htm>.]
- Bryant, W. A. (1988), Owens Valley fault zone, Inyo County, in *California Division of Mines and Geology Fault Evaluation Reports, FER-192*, Calif. Geol. Surv., reprinted in *Division of Mines and Geology Open-File Report, 90-14*. [Available at <http://www.quake.ca.gov/gmaps/WH/regulatorymaps.html>.]
- Candela, T., F. Renard, M. Bouchon, J. Schmittbuhl, and E. E. Brodsky (2011), Stress drop during earthquakes: Effect of fault roughness scaling, *Bull. Seismol. Soc. Am.*, 101(5), 2369–2387, doi:10.1785/0120100298.
- Carver, G. A. (1970), Quaternary tectonism and surface faulting in Owens Lake basin, Reno, California, *Tech. Rep. AT2*, 103 pp., Mackay Sch. of Mines, Univ. of Nev., Reno.
- Caskey, S. J., S. G. Wesnousky, P. Zhang, and D. B. Slemmons (1996), Surface faulting of the 1954 Fairview Peak (MS 7.2) and Dixie Valley (MS 6.8) earthquakes, central Nevada, *Bull. Seismol. Soc. Am.*, 86(3), 761–787.
- Chen, T., S. O. Akçiz, K. W. Hudnut, D. Z. Zhang, and J. M. Stock (2015), Fault-slip distribution of the 1999 Mw 7.1 Hector Mine earthquake, California, estimated from postearthquake airborne LiDAR data, *Bull. Seismol. Soc. Am.*, 105, 15, 776–790, doi:10.1785/0120130108.
- Cochran, E. S., Y. G. Li, P. M. Shearer, S. Barbot, Y. Fialko, and J. E. Vidale (2009), Seismic and geodetic evidence for extensive, long-lived fault damage zones, *Geology*, 37, 315–318, doi:10.1130/G25306A.1.
- Cowgill, E. (2007), Impact of riser reconstructions on estimation of secular variation in rates of strike-slip faulting: Revisiting the Charchen River site along the Altyn Tagh fault, NW China, *Earth Planet. Sci. Lett.*, 254(3–4), 239–255, doi:10.1016/j.epsl.2006.09.015.
- dePolo, C. M. (1989), Seismotectonics of the White Mountains fault system, east-central California and west-central Nevada, MS thesis, Univ. of Nev., Reno.
- dePolo, C. M., D. G. Clark, D. B. Slemmons, and A. R. Ramelli (1991), Historical surface faulting in the Basin and Range province, western North America: Implications for fault segmentation, *J. Struct. Geol.*, 13(2), 123–136, doi:10.1016/0191-8141(91)90061-M.
- Dixon, T. H., S. Robaudo, J. Lee, and M. Reheis (1995), Constraints on present-day basin and range deformation from space geodesy, *Tectonics*, 14(4), 755–772, doi:10.1029/95TC00931.
- Dixon, T. H., E. Norabuena, and L. Hotelling (2003), Paleoseismology and global positioning system: Earthquake-cycle effects and geodetic versus geologic fault slip rates in the eastern California shear zone, *Geology*, 31, 55–58, doi:10.1130/0091-7613(2003)031<0055:PAG-PSE>2.0.CO;2.
- Dokka, R. K., and C. J. Travis (1990), Role of the eastern California shear zone in accommodating Pacific–North American Plate motion, *Geophys. Res. Lett.*, 17(9), 1323–1326, doi:10.1029/GL017i009p01323.
- Duffy, B., M. Quigley, D. J. A. Barrell, R. Van Dissen, T. Stahl, S. Leprince, C. McInnes, and E. Bilderback (2013), Fault kinematics and surface deformation across a releasing bend during the 2010 MW 7.1 Darfield, New Zealand, earthquake revealed by differential LiDAR and cadastral surveying, *Geol. Soc. Am. Bull.*, 125(3/4), 420–431, doi:10.1130/B30753.1.
- Dühnforth, M., A. L. Densmore, S. Ivy-Ochs, P. A. Allen, and P. W. Kubik (2007), Timing and patterns of debris flow deposition on Shepherd and Symmes creek fans, Owens Valley, California, deduced from cosmogenic <sup>10</sup>Be, *J. Geophys. Res.*, 112, F03S15, doi:10.1029/2006JF000562.
- Elliott, A. J., J. F. Dolan, and D. D. Oglesby (2009), Evidence from coseismic slip gradients for dynamic control on rupture propagation and arrest through stepovers, *J. Geophys. Res.*, 114, B02313, doi:10.1029/2008JB005969.
- Fletcher, J. M., et al. (2014), Assembly of a large earthquake from a complex fault system: Surface rupture kinematics of the 4 April 2010 El Mayor–Cucapah (Mexico) Mw 7.2 earthquake, *Geosphere*, 10(4), 797–827.
- Foy, T. A., K. L. Frankel, Z. M. Lifton, C. W. Johnson, and M. W. Caffee (2012), Distributed extensional deformation in a zone of right-lateral shear: Implications for geodetic versus geologic rates of deformation in the eastern California shear zone–Walker Lane, *Tectonics*, 31, TC4008, doi:10.1029/2011TC002930.
- Frankel, K. L., J. F. Dolan, R. C. Finkel, L. A. Owen, and J. S. Hoeft (2007a), Spatial variations in slip rate along the Death Valley–Fish Lake Valley fault system determined from LiDAR topographic data and cosmogenic <sup>10</sup>Be geochronology, *Geophys. Res. Lett.*, 34, L18303, doi:10.1029/2007GL030549.
- Frankel, K. L., et al. (2007b), Cosmogenic <sup>10</sup>Be and <sup>36</sup>Cl geochronology of offset alluvial fans along the northern Death Valley fault zone: Implications for transient strain in the eastern California shear zone, *J. Geophys. Res.*, 112, B06407, doi:10.1029/2006JB004350.
- Ganev, P. N., J. F. Dolan, K. L. Frankel, and R. C. Finkel (2010), Rates of extension along the Fish Lake Valley fault and transtensional deformation in the eastern California shear zone–Walker Lane belt, *Lithosphere*, 2(1), 33–49, doi:10.1130/L51.1.

- Gilbert, G. K. (1884), A theory of earthquakes of the Great Basin, with a practical application, *Am. J. Sci.*, 29, 49–53.
- Gold, P. O., M. E. Oskin, A. J. Elliott, A. Hinojosa-Corona, M. H. Taylor, O. Kreylos, and E. Cowgill (2013), Coseismic slip variation assessed from terrestrial LiDAR scans of the El Mayor-Cucupah surface rupture, *Earth Planet. Sci. Lett.*, 366, 151–162, doi:10.1016/j.epsl.2013.01.040.
- Gold, R. D., and E. Cowgill (2011), Deriving fault-slip histories to test for secular variation in slip, with examples from the Kunlun and Awatere faults, *Earth Planet. Sci. Lett.*, 301(1), 52–64, doi:10.1016/j.epsl.2010.10.011.
- Gold, R. D., N. G. Reitman, R. W. Briggs, W. D. Barnhart, and G. Hayes (2015), On- and off-fault deformation associated with the September 2013 Mw7.7 Balochistan earthquake: Implications for geologic slip rate measurements, *Tectonophysics*, 660, 65–78, doi:10.1016/j.tecto.2015.08.019.
- Griffith, W., G. Di Toro, G. Pennacchioni, D. Pollard, and S. Nielsen (2009), Static stress drop associated with brittle slip events on exhumed faults, *J. Geophys. Res.*, 114, B02402, doi:10.1029/2008JB005879.
- Gupta, A., and C. H. Scholz (2000), Brittle strain regime transition in the Afar depression: Implications for fault growth and seafloor spreading, *Geology*, 28(12), 1087–1090.
- Haeussler, P. J., et al. (2004), Surface rupture and slip distribution of the Denali and Totschunda faults in the 3 November 2002 M 7.9 earthquake, Alaska, *Bull. Seismol. Soc. Am.*, 94(6B), S23–S52, doi:10.1785/0120040626.
- Hanks, T. C., and W. H. Bakun (2002), A bilinear source-scaling model for M-log a observations of continental earthquakes, *Bull. Seismol. Soc. Am.*, 92, 1841–1846, doi:10.1785/0120010148.
- Hanks, T. C., and H. Kanamori (1979), A moment magnitude scale, *J. Geophys. Res.*, 84(B5), 2348–2350.
- Hauksson, E., and P. Shearer (2005), Southern California hypocenter relocation with waveform cross-correlation, part 1: Results using the double-difference method, *Bulletin of the Seismological Society of America*, 95(3), 896–915, doi:10.1785/0120040167.
- Hecker, S., T. E. Dawson, and D. P. Schwartz (2010), Normal-faulting slip maxima and stress-drop variability: A geological perspective, *Bull. Seismol. Soc. Am.*, 100(6), 3130–3147, doi:10.1785/0120090356.
- Henry, C. D., J. E. Faulds, and C. M. dePolo (2007), Geometry and timing of strike-slip and normal faults in the northern Walker Lake, northwestern Nevada and northeastern California: Strain partitioning or sequential extensional and strike-slip?, *Spec. Pap. Geol. Soc. Am.*, 434, 59–79.
- Hobbs, W. H. (1910), The earthquake of 1872 in the Owens Valley, California, *J. Soc. Pet. Geophys.*, 10, 352–385.
- Hough, S. E., and K. Hutton (2008), Revisiting the 1872 Owens Valley California earthquake, *Bull. Seismol. Soc. Am.*, 98(2), 931–949, doi:10.1785/0120070186.
- Jayko, A. S., and S. N. Bacon (2008), Late Quaternary MIS 6–8 shoreline, Owens Valley, eastern California, *Spec. Pap. Geol. Soc. Am.*, 439, 185–206, doi:10.1130/2008.2439(07).
- Jayko, A. S., and M. Bursik (2012), Active transtensional intracontinental basins, Walker Lane, western Great Basin, in *Tectonics of Sedimentary Basins*, edited by C. Busby and A. Antonio, pp. 226–248, Wiley-Blackwell, West Sussex, U. K.
- Kanamori, H., and C. R. Allen (1986), Earthquake repeat time and average stress drop, in *Earthquake Source Mechanics*, vol. 37, edited by S. Das, J. Boatwright, and C. H. Scholz, pp. 227–236, AGU, Washington, D. C.
- Kirby, E., D. W. Burbank, M. Reheis, and F. Phillips (2006), Temporal variations in slip rate of the White Mountain fault zone, eastern California, *Earth Planet. Sci. Lett.*, 248, 168–185, doi:10.1016/j.epsl.2006.05.026.
- Kirby, E., S. Anandakrishnan, F. Phillips, and S. Marrero (2008), Late Pleistocene slip rate along the Owens Valley fault, eastern California, *Geophys. Res. Lett.*, 35, L01304, doi:10.1029/2007GL031970.
- Klinger, Y. (2010), Relation between continental strike-slip earthquake segmentation and thickness of the crust, *J. Geophys. Res.*, 115, B07306, doi:10.1029/2009JB006550.
- Klinger, Yann, R. Michel, and G.C.P. King (2006), Evidence for an earthquake barrier model from Mw ~7.8 Kokoxili (Tibet) earthquake slip-distribution, *Earth Planet. Sci. Lett.*, 242.3, 354–364, doi:10.1016/j.epsl.2005.12.003.
- Klinger, Y., M. Etchebes, P. Tapponnier, and C. Narteau (2011), Characteristic slip for five great earthquakes along the Fuyun fault in China, *Nat. Geosci.*, 4, 389–392, doi:10.1038/ngeo1158.
- Knapp, C., and G. C. Carter (1976), The generalized correlation method for estimation of time delay, *IEEE Trans. Acoust. Speech Signal Process.*, 24(4), 320–327.
- Koehler, P. A., and R. S. Anderson (1994), Full-glacial shoreline vegetation during the maximum highstand at Owens Lake, California, *Great Basin Nat.*, 54, 142–149.
- Le, K., J. Lee, L. A. Owen, and R. Finkel (2007), Late Quaternary slip rates along the Sierra margin of the eastern California shear zone/Basin and Range province, *Geol. Soc. Am. Bull.*, 119, 240–256, doi:10.1130/B25960.1.
- Lee, J., J. Spencer, and L. Owen (2001a), Holocene slip rates along the Owens Valley fault, California: Implications for the recent evolution of the eastern California shear zone, *Geology*, 29(9), 819–822, doi:10.1130/00917613(2001)029 <0819:HSRATO>2.0.CO;2.
- Lee, J., C. M. Rubin, and A. Calvert (2001b), Quaternary faulting history along the Deep Springs fault, California, *Geol. Soc. Am. Bull.*, 113(7), 855–869, doi:10.1130/0016-7606(2001)113 <0855:QFHATD>2.0.CO;2.
- Lienkaemper, J. J. (2001), 1857 slip on the San Andreas Fault southeast of Cholame, California, *Bull. Seismol. Soc. Am.*, 91(6), 1659–1672.
- Lifton, Z. M., A. V. Newman, K. L. Frankel, C. W. Johnson, and T. H. Dixon (2013), Insights into distributed plate rates across the Walker Lane from GPS geodesy, *Geophys. Res. Lett.*, 40, 4620–4624, doi:10.1002/grl.50804.
- Lubetkin, L. K. C., and M. M. Clark (1988), Late Quaternary activity along the Lone Pine fault, eastern California, *Geol. Soc. Am. Bull.*, 100(5), 755–766, doi:10.1130/0016-7606(1988)100 <0755:LQAATL>2.3.CO;2.
- Ludwig, L. G., S. O. Akçiz, G. R. Noriega, O. Zielke, and J. R. Arrowsmith (2010), Climate-modulated channel incision and rupture history of the San Andreas fault in the Carrizo Plain, *Science*, 327(5969), 1117–1119, doi:10.1126/science.1182837.
- Madden, C., D. E. Haddad, J. B. Salisbury, O. Zielke, J. R. Arrowsmith, R. J. Weldon, and J. Colunga (2013), Appendix R—Compilation of slip-in-the-last-event data and analysis of last event, repeated slip, and average displacement for recent and prehistoric ruptures, *U.S. Geol. Surv. Open File Rep.*, 1165, 65 pp.
- Manighetti, I., M. Campillo, C. Sammis, P. M. Mai, and G. King (2005), Evidence for self-similar, triangular slip distributions on earthquakes: Implications for earthquake and fault mechanics, *J. Geophys. Res.*, 110, B05302, doi:10.1029/2004JB003174.
- McAuliffe, L. J., J. F. Dolan, E. Kirby, C. Rollins, B. Haravitch, S. Alm, and T. M. Rittenour (2013), Paleoseismology of the southern Panamint Valley fault: Implications for regional earthquake occurrence and seismic hazard in southern California, *J. Geophys. Res. Solid Earth*, 118, 5126–5146, doi:10.1002/jgrb.50359.
- McCalpin, J. P., and D. B. Slemmons (1998), Statistics of paleoseismic data, final technical report, U.S. Geological Survey National Earthquake Hazards Reduction Program, Final Technical Report, Contract 1434-HQ-96-GR-02752, 62 pp. [Available at [http://works.bepress.com/james\\_mccalpin/12/](http://works.bepress.com/james_mccalpin/12/)]
- McGill, S. F., and C. M. Rubin (1999), Surficial slip distribution on the central Emerson fault during the June 28, 1992, Landers earthquake, California, *J. Geophys. Res.*, 104(B3), 4811–4833, doi:10.1029/98JB01556.

- McGill, S. F., and K. Sieh (1991), Surficial offsets on the eastern Garlock fault associated with prehistoric earthquakes, *J. Geophys. Res.*, *96*(21), 597–621, doi:10.1029/91JB02030.
- Mendoza, C. (1993), Coseismic slip of two large Mexican earthquakes from teleseismic body waveforms: Implications for asperity interaction in the Michoacan plate boundary segment, *J. Geophys. Res.*, *98*(B5), 8197–8210.
- Milliner, C. W., J. F. Dolan, J. Hollingsworth, S. Leprince, F. Ayoub, and C. G. Sammis (2015), Quantifying near-field and off-fault deformation patterns of the 1992 Mw 7.3 Landers earthquake, *Geochem. Geophys. Geosyst.*, *16*, 1577–1598, doi:10.1002/2014GC005693.
- Monastero, F. C., J. D. Walker, A. M. Katzenstein, and A. E. Sabin (2002), Neogene evolution of the Indian Wells Valley, east-central California: Geologic evolution of the Mojave Desert and southwestern Basin and Range, *Geol. Soc. Am. Mem.*, *195*, 199–228, doi:10.1130/0-8137-1195-9.199.
- Nagorsen-Rinke, S., J. Lee, and A. Calvert (2013), Pliocene sinistral slip across the Adobe Hills, eastern California–western Nevada: Kinematics of fault slip transfer across the Mina deflection, *Geosphere*, *9*, 37–53, doi:10.1130/GES00825.1.
- Orme, A. J., and A. R. Orme (2008), Late Pleistocene climate and tectonic impacts on Owens Lake levels and linkages, *Spec. Pap. Geol. Soc. Am.*, *439*, 207–225.
- Oskin, M., L. Perg, D. Blumentritt, S. Mukhopadhyay, and A. Iriondo (2007), Slip rate of the Calico fault: Implications for geologic versus geodetic rate discrepancy in the eastern California shear zone, *J. Geophys. Res.*, *112*, B03402, doi:10.1029/2006JB004451.
- Oskin, M. E., et al. (2012), Near-field deformation from the El Mayor-Cucapah earthquake revealed by differential LiDAR, *Science*, *335*, 335–337.
- Oswald, J. A., and S. G. Wesnousky (2002), Neotectonics and Quaternary geology of the Hunter Mountain fault zone and Saline Valley region, southeastern California, *Geomorphology*, *42*(3), 255–278, doi:10.1016/S0169-555X(01)00089-7.
- Ozacar, A. A., and S. L. Beck (2004), The 2002 Denali fault and 2001 Kunlun fault earthquakes: Complex rupture processes of two large strike-slip events, *Bull. Seismol. Soc. Am.*, *94*(6B), S278–S292.
- Phillips, F. M., and L. Majkowski (2011), The role of low-angle normal faulting in active tectonics of the northern Owens Valley, California, *Lithosphere*, *3*(1), 22–36, doi:10.1130/L73.1.
- Price, E., and R. Bürgmann (2002), Interactions between the Landers and Hector Mine, California, earthquakes from space geodesy, boundary element modeling, and time-dependent friction, *Bull. Seismol. Soc. Am.*, *92*, 1450–1469, doi:10.1785/0120000924.
- Quigley, M., R. Van Disson, N. Litchfield, P. Villamor, B. Duffy, D. Barrell, K. Furlong, T. Stahl, E. Bilderback, and D. Noble (2012), Surface rupture during the 2010 Mw 7.1 Darfield (Canterbury) earthquake: Implications for fault rupture dynamics and seismic-hazard analysis, *Geology*, *40*(1), 55–58, doi:10.1130/G32528.1.
- Reheis, M. C., and T. H. Dixon (1996), Kinematics of the eastern California shear zone: Evidence for slip transfer from Owens and Saline Valley fault zones to Fish Lake Valley fault zone, *Geology*, *24*(4), 339–342, doi:10.1130/00917613(1996)024 <0339:KOTECES>2.3.CO;2.
- Reheis, M. C., and T. L. Sawyer (1997), Late Cenozoic history and slip rates of the Fish Lake Valley, Emigrant Peak, and Deep Springs fault zones, Nevada and California, *Geol. Soc. Am. Bull.*, *109*(3), 280–299, doi:10.1130/0016-7606(1997)109 <0280:LCHASR>2.3.CO;2.
- Rockwell, T. K., and Y. Klinger (2013), Surface rupture and slip distribution of the 1940 Imperial Valley earthquake, Imperial fault, southern California: Implications for rupture segmentation and dynamics, *Bull. Seismol. Soc. Am.*, *103*(2A), 629–640, doi:10.1785/0120120192.
- Rockwell, T. K., S. Lindvall, M. Herzberg, D. Murbach, T. Dawson, and G. Berger (2000), Paleoseismology of the Johnson Valley, Kickapoo, and Homestead Valley faults: Clustering of earthquakes in the eastern California shear zone, *Bull. Seismol. Soc. Am.*, *90*, 1200–1236, doi:10.1785/0119990023.
- Rockwell, T. K., S. Lindvall, T. Dawson, R. Langridge, W. Lettis, and Y. Klinger (2002), Lateral offsets on surveyed cultural features resulting from the 1999 Izmit and Düzce earthquakes, Turkey, *Bull. Seismol. Soc. Am.*, *92*(1), 79–94, doi:10.1785/0120000809.
- Rodgers, D. W., and T. A. Little (2006), World's largest coseismic strike-slip offset: The 1855 rupture of the Wairarapa fault, New Zealand, and implications for displacement/length scaling of continental earthquakes, *J. Geophys. Res.*, *111*, B12408, doi:10.1029/2005JB004065.
- Salisbury, J. B., T. K. Rockwell, T. J. Middleton, and K. W. Hudnut (2012), LiDAR and field observations of slip distribution for the most recent surface ruptures along the central San Jacinto fault, *Bull. Seismol. Soc. Am.*, *102*(2), 598–619, doi:10.1785/0120110068.
- Sauber, J., W. Thatcher, S. C. Solomon, and M. Lisowski (1994), Geodetic slip rate for the eastern California shear zone and the recurrence time of Mojave Desert earthquakes, *Nature*, *367*, 264–266.
- Scharer, K. M., J. B. Salisbury, J. R. Arrowsmith, and T. K. Rockwell (2014), Southern San Andreas fault evaluation field activity: Approaches to measuring small geomorphic offsets—Challenges and recommendations for active fault studies, *Seismol. Res. Lett.*, *85*(1), 68–76, doi:10.1785/0220130108.
- Scholz, C. H., and T. M. Lawler (2004), Slip tapers at the tips of faults and earthquake ruptures, *Geophys. Res. Lett.*, *31*, L21609, doi:10.1029/2004GL021030.
- Scholz, C. H., C. A. Aviles, and S. G. Wesnousky (1986), Scaling differences between large interpolate and intraplate earthquakes, *Bull. Seismol. Soc. Am.*, *76*, 65–70.
- Schwartz, D., and K. Coppersmith (1984), Fault behavior and characteristic earthquakes: Examples from the Wasatch and San Andreas fault zones, *J. Geophys. Res.*, *89*(B7), 1421–1448, doi:10.1029/JB089iB07p05681.
- Sieh, K., and R. Jahns (1984), Holocene activity of the San Andreas fault at Wallace Creek, California, *Geol. Soc. Am. Bull.*, *95*, 883–896, doi:10.1130/0016-7606(1984)95 <883:HAOTSA>2.0.CO;2.
- Sieh, K., et al. (1993), Near-field investigations of the Landers earthquake sequence, April to July 1992, *Science*, *260*(5105), 171–176, doi:10.1126/science.260.5105.171.
- Sieh, K. E. (1978), Slip along the San Andreas fault associated with the great 1857 earthquake, *Bull. Seismol. Soc. Am.*, *68*(5), 1421–1448.
- Slemmons, D. B., E. Vittori, A. S. Jayko, G. A. Carver, and S. N. Bacon (2008), Quaternary fault and lineament map of Owens Valley, Inyo County, eastern California, *Map Chart 96*, 25 pp., Geol. Soc. of Am., doi:10.1130/2008.MCH096.
- Smith, G. I., and J. L. Bischoff (1997), An 800,000-year paleoclimatic record from core OL-92, Owens Lake, southeast California: Boulder, Colorado, *Spec. Pap. Geol. Soc. Am.*, *317*, 8, 166 pp.
- Stein, R. S., and T. C. Hanks (1998), Mw6 earthquakes in southern California during the twentieth century: No evidence for a seismicity or moment deficit, *Bull. Seismol. Soc. Am.*, *88*, 635–652.
- Stewart, J. H. (1988), Tectonics of the Walker Lane belt, western Great Basin Mesozoic and Cenozoic deformation in a zone of shear, in *Metamorphism and Crustal Evolution of the Western US*, vol. VII, edited by W. G. Ernst, pp. 685–713, Prentice Hall, Englewood Cliffs, N. J.
- Stirling, M., D. Rhoades, and K. Berryman (2002), Comparison of earthquake scaling relations derived from data of the instrumental and preinstrumental era, *Bull. Seismol. Soc. Am.*, *92*, 812–830, doi:10.1785/0120000221.
- Stirling, M., T. Goded, K. Berryman, and N. Litchfield (2013), Selection of earthquake scaling relationships for seismic-hazard analysis, *Bull. Seismol. Soc. Am.*, *103*(6), 1–19, doi:10.1785/0120130052.
- Teran, O. J., J. M. Fletcher, M. E. Oskin, T. K. Rockwell, K. W. Hudnut, R. M. Spelz, S. O. Akciz, A. P. Hernandez-Flores, and A. E. Morelan (2015), Geologic and structural controls on rupture zone fabric: A field-based study of the 2010 Mw 7.2 El Mayor–Cucapah earthquake surface rupture, *Geosphere*, *11*(3), 899–920, doi:10.1130/GES01078.1.

- Thompson, S. C., R. J. Weldon, C. M. Rubin, K. Abdрахmatov, P. Molnar, and G. W. Berger (2002), Late Quaternary slip rates across the central Tien Shan, Kyrgyzstan, central Asia, *J. Geophys. Res.*, *107*(B9), 2203, doi:10.1029/2001JB000596.
- Treiman, J. A., K. J. Kendrick, W. A. Bryant, T. K. Rockwell, and S. F. McGill (2002), Primary surface rupture associated with the Mw 7.1 16 October 1999 Hector Mine earthquake, San Bernardino County, California, *Bull. Seismol. Soc. Am.*, *92*(4), 1171–1191, doi:10.1785/0120000923.
- Turrin, B., and A. R. Gillespie (1986), K/Ar ages of basaltic volcanism of the big pine volcanic field, California: Implications for glacial stratigraphy and neotectonics of the Sierra Nevada, *Geol. Soc. Am. Abstr. Programs*, *18*(6), 777.
- Unruh, J., J. Humphrey, and A. Barron (2003), Transtensional model of Sierra Nevada frontal fault system, eastern California, *Geology*, *31*, 327–330, doi:10.1130/00917613(2003)031<0327:TMFTSN>2.0.CO;2.
- Unruh, J., E. Hauksson, and C. H. Jones (2014), Internal deformation of the southern Sierra Nevada microplate associated with foundering lower lithosphere, California, *Geosphere*, *10*(1), 107–128, doi:10.1130/GES00936.1.
- Unruh, J. R., E. Hauksson, F. C. Monastero, R. J. Twiss, and J. C. Lewis (2002), Seismotectonics of the Coso Range-Indian Wells Valley region, California: Transtensional deformation along the southeastern margin of the Sierran microplate, *Geol. Soc. Am. Mem.*, *195*, 277–294, doi:10.1130/0-8137-1195-9.277.
- U.S. Geological Survey, the Southern California Earthquake Center, and the California Division of Mines and Geology (2000), Preliminary report on the 16 October 1999 M7.1 Hector Mine, California, earthquake, *Seismol. Res. Lett.*, *71*, 11–23.
- Vittori, E., A. M. Michetti, D. B. Slemmons, and G. Carver (1993), Style of recent surface deformation at the south end of the Owens Valley fault zone, eastern California, *Geol. Soc. Am. Abstr. Programs*, *25*(5), 159.
- Wallace, R. E. (1968), Notes on stream channels offset by the San Andreas fault, southern Coast Ranges, California, *Stanford Univ. Publ. Geol. Sci.*, *11*, 6–20.
- Ward, S. N. (1997), Dogtails versus rainbows: Synthetic earthquake rupture models as an aid in interpreting geological data, *Bull. Seismol. Soc. Am.*, *87*, 1422–1441.
- Weldon, R. J., J. P. McCalpin, and T. K. Rockwell (1996), Paleoseismology of strike-slip tectonic environments, in *Paleoseismology, Int. Geophys. Ser.*, vol. 62, edited by J. P. McCalpin, pp. 33–83, Academic, N. Y.
- Wells, D., and K. Coppersmith (1994), New empirical relationships among magnitude, rupture length, rupture width, rupture area, and surface displacement, *Bull. Seismol. Soc. Am.*, *84*, 974–1002.
- Wesnousky, S. G. (1988), Seismological and structural evolution of strike-slip faults, *Nature*, *335*, 340–343.
- Wesnousky, S. G. (2005), Active faulting in the Walker Lane, *Tectonics*, *24*, TC3009, doi:10.1029/2004TC001645.
- Wesnousky, S. G. (2008), Displacement and geometrical characteristics of earthquake surface ruptures: Issues and implications for seismic hazard analysis and process of earthquake rupture, *Bull. Seismol. Soc. Am.*, *98*(4), 1609–1632, doi:10.1785/0120070111.
- Wesnousky, S. G., and C. H. Jones (1994), Oblique slip, slip partitioning, spatial and temporal changes in the regional stress field, and the relative strength of active faults in the basin and range, western United States, *Geology*, *22*(11), 1031–1034, doi:10.1130/00917613(1994)022<1031:OSSPSA>2.3.CO;2.
- Wesnousky, S. G., J. M. Bormann, C. Kreemer, W. C. Hammond, and J. N. Brune (2012), Neotectonics, geodesy, and seismic hazard in the northern Walker Lane of western North America: Thirty kilometers of crustal shear and no strike-slip?, *Earth Planet. Sci. Lett.*, *329*–*330*, 133–140, doi:10.1016/j.epsl.2012.02.018.
- Whitney, J. D. (1872a), The Owens Valley earthquake, Part I, *Overland Mon.*, *9*, 130–140.
- Whitney, J. D. (1872b), The Owens Valley earthquake, Part II, *Overland Mon.*, *9*, 266–278.
- Winograd, I. J., J. M. Landwehr, T. B. Copen, W. D. Sharp, A. C. Riggs, K. R. Ludwig, and P. T. Kolesar (2006), Devils Hole, Nevada, <sup>18</sup>O record extended to the mid-Holocene, *Quat. Res.*, *66*, 202–212, doi:10.1016/j.yqres.2006.06.003.
- Zachariesen, J., and K. E. Sieh (1995), The transfer of slip between two en echelon strike-slip faults: A case study from the 1992 Landers earthquake, southern California, *J. Geophys. Res.*, *100*(B8), 15,281–15,301.
- Zehfuss, P. H., P. R. Bierman, A. R. Gillespie, R. M. Burke, and M. W. Caffee (2001), Slip rates on the Fish Springs fault, Owens Valley, California, deduced from cosmogenic <sup>10</sup>Be and <sup>26</sup>Al and soil development on fan surfaces, *Geol. Soc. Am. Bull.*, *113*(2), 241–255, doi:10.1130/0016-7606(2001)113<0241:SROTFS>2.0.CO;2.
- Zielke, O., and J. R. Arrowsmith (2012), LaDiCaoz and LiDARimager—MATLAB GUIs for LiDAR data handling and lateral displacement measurement, *Geosphere*, *8*(1), 206–221, doi:10.1130/GES00686.1.
- Zielke, O., J. R. Arrowsmith, L. G. Ludwig, and S. O. Akçiz (2010), Slip in the 1857 and earlier large earthquakes along the Carrizo Plain, San Andreas Fault, *Science*, *327*(5969), 1119–1122, doi:10.1126/science.1182781.
- Zielke, O., J. R. Arrowsmith, L. G. Ludwig, and S. O. Akçiz (2012), High resolution topography derived offsets along the 1857 Fort Tejon earthquake rupture trace, San Andreas Fault, *Bull. Seismol. Soc. Am.*, *102*(3), 1135–1154, doi:10.1785/0120110230.
- Zielke, O., Y. Klinger, and J. R. Arrowsmith (2015), Fault slip and earthquake recurrence along strike-slip faults—Contributions of high-resolution geomorphic data, *Tectonophysics*, *638*, 43–62, doi:10.1016/j.tecto.2014.11.004.